

# FreeCond: Free Lunch in the Input Conditions of Text-Guided Inpainting

Teng-Fang Hsiao, Bo-Kai Ruan, Sung-Lin Tsai, Yi-Lun Wu, Hong-Han Shuai

National Yang Ming Chiao Tung University

tfhsiao.ee13@nycu.edu.tw, bkruan.ee11@nycu.edu.tw, tsai412504004.ee12@nycu.edu.tw

yilun.ee08@nycu.edu.tw, hhshuai@nycu.edu.tw



Figure 1. Comparison of T2I inpainting methods with FreeCond, applied across various mask types: “multi-masks” (column 1 and 4), “precise masks” (columns 2, 5, and 6), and “rough masks” (columns 3 and 7) with complex prompts and unrelated image contexts. By integrating FreeCond, existing inpainting baselines obtain better “instruction-following” performance.

## Abstract

In this study, we aim to determine and solve the deficiency of Stable Diffusion Inpainting (SDI) in following the instruction of both prompt and mask. Due to the training bias from masking, the inpainting quality is hindered when the prompt instruction and image condition are not related. Therefore, we conduct a detailed analysis of the internal representations learned by SDI, focusing on how the mask input influences the cross-attention layer. We observe that adapting text key tokens toward the input mask enables the model to selectively paint within the given area. Leveraging these insights, we propose FreeCond, which adjusts only the input mask condition and image condition. By increasing the latent mask value and modifying the frequency of image condition, we align the cross-attention features with the

model’s training bias to improve generation quality without additional computation, particularly when user inputs are complicated and deviate from the training setup. Extensive experiments demonstrate that FreeCond can enhance any SDI-based model, e.g., yielding up to a 60% and 58% improvement of SDI and SDXL in the CLIP score. Our work is publicly available at <https://github.com/BlueDyee/FreeCond>.

## 1. Introduction

Text-to-image (T2I) inpainting seeks to fill specified masked areas based on user-provided text prompts. Stable Diffusion Inpainting (SDI), a tailored adaptation of Stable Diffusion [26], is widely used for its effectiveness in achieving high-quality inpainting aligned with text

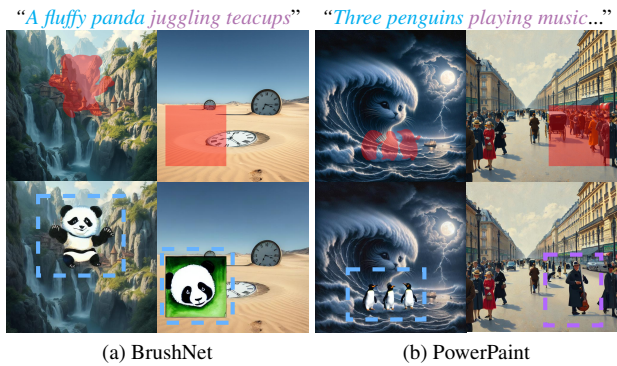


Figure 2. Comparison of existing SOTA methods. BrushNet rigidly follows the mask instructions but only partially adheres to the prompt. PowerPaint produces outputs that are harmonious with the image context but at the cost of reduced prompt-adherence. FreeCond addresses these limitations, as shown in Fig. 1.

prompts. However, the SDI training process employs a random masking strategy, which often hinders the model’s ability to follow prompts accurately and fit masks precisely, especially when the prompt lacks contextual relevance to the surrounding image. We refer to these dual issues of “prompt-adherence” and “mask-fitting” collectively as the “instruction-following” problem: the model prioritizes contextual coherence over generating content that strictly adheres to both the complex prompt details and the user-specified mask, as illustrated in the second row of Fig. 1.

To address these limitations, methods such as HD-Painter [20], BrushNet [13], and PowerPaint [42] have been developed. BrushNet, for example, leverages segmentation-based training data and a ControlNet-like structure, allowing it to learn a direct link between the input mask and prompt. PowerPaint incorporates training with dilated segmentation masks and task-specific tokens, enabling flexible object inpainting that better conforms to varied shapes. While these approaches effectively reduce the “mask-fitting” issue, they primarily optimize for simple prompts and often lack the generalization capability required for complex prompt adherence, as shown in Fig. 2. Observing the limitations of training-only modifications, we propose to directly modify the model’s behavior by adjusting its learned mechanism.

In this paper, we contend that effective instruction-following relies on the differential noise predictions: *conditional versus unconditional*, modulated via classifier-free guidance (CFG) [9]. This differential is notably manifested in the outputs of the cross-attention layer, where prompt tokens receive significantly higher attention within the masked area than in surrounding regions. Consequently, the query and key features within the cross-attention layer must dynamically adapt to the input mask. This adaptation focuses on generating coherent new content within the masked regions while concurrently preserving the integrity

of the surrounding context by selectively enhancing features related to the mask in the corresponding channels.

To address these challenges, we propose FreeCond, a training-free method that requires no extra computation. Specifically, FreeCond filters the high-frequency components of the image condition in the early diffusion steps, reducing the contextual information of the image condition. Furthermore, FreeCond induces a stronger feature shift in the cross-attention layer by scaling the mask condition, enabling stronger activation of the masked area. By adjusting the input conditions, FreeCond significantly enhances both prompt-adherence and mask-fitting while preserving overall harmony. Notably, FreeCond, as a more general form of noise prediction function, can be seamlessly integrated with other SDI-based methods [13, 20, 23, 39, 42], as it directly enhances the original SDI backbone.

Finally, we propose FCIBench (FreeCond Inpainting Benchmark), a new benchmark with 600 inpainting pairs, to handle complex inpainting scenarios. Compared with existing inpainting benchmarks [13, 16], FCIBench includes precise masks, rough masks, and multi-masks, along with complex prompts that are unrelated to image condition, as shown in the first row of Fig. 1. This variety enables a more comprehensive evaluation of SDI across diverse inpainting conditions. Our expanded benchmark thus helps a thorough assessment of the performance of different models across varied prompts and mask configurations. Experimental results demonstrate that FreeCond consistently improves performance across models and benchmarks, achieving a 60% increase in CLIP score [24] of SDI backbone and a 1% increase of existing SOTA. The contributions can be summarized as follows.

- We conduct an in-depth analysis of the SDI model’s mechanism, enhancing the interpretability by examining its learned bias of relying on image context and its capability to selectively inpaint within the masked area.
- We introduce FreeCond, a novel noise prediction function, that addresses the instruction-following limitations of SDI-based models without adding computational overhead, especially in scenarios where the complex prompt instruction is unrelated to the image condition.
- We provide FCIBench to evaluate inpainting methods in scenarios across precise mask, rough mask, and multi-mask settings, along with complex prompts that are unrelated to image conditions, extending the evaluation to more diverse scenarios.

## 2. Related Works

### 2.1. Image Inpainting

Image inpainting focuses on repainting specified regions while ensuring coherence with the surrounding image. Various non-text-guided inpainting methods have been devel-

oped to achieve this [4, 12, 18, 22, 36–38, 41], alongside the emergence of text-to-image inpainting methods [1, 21, 25, 29, 33, 39]. SDI [26] pioneered the integration of a random masking strategy into its training objective, producing harmonized outputs. However, this approach often prioritizes image conditioning over adherence to instructions. To improve this, recent methods [13, 20, 31, 42] have introduced solutions focused primarily on enhancing mask-fitting. Despite these advancements, these methods often lack prompt-adherence when handling complex instructions. In contrast, FreeCond leverages insights into the inpainting mechanism to improve instruction-following across any SDI-based inpainting model, achieving a balanced performance between mask-fitting and prompt-adherence.

## 2.2. Unveiling the Mechanism of T2I Models

T2I diffusion models possess powerful image-generation capabilities. To fully harness this potential, recent works have explored various training-free modifications based on in-depth analyses of different components [3, 5–8, 10, 11, 17, 19, 34, 35]. Notably, FreeU [28] reveals that the skip-connection primarily retains texture details, while the backbone captures more semantic information. By adjusting the balance between them, FreeU enhances semantic accuracy with minimal impact on detail and computational costs.

Our analysis reveals that the image and mask conditions play similar roles: the image condition provides contextual details, while the mask condition regulates prompt influence. By modulating both conditions, we achieve improved instruction-following without additional costs, providing a “free lunch” in performance enhancement.

## 3. Analysis of SDI model

In this section, we provide an in-depth analysis of the SDI model. Firstly, we identify the training bias of the SDI model in Sec. 3.2 that the model heavily relies on the image condition to generate the content. This mechanism can cause the generated output unrelated to the input prompt. Secondly, we demonstrate in Sec. 3.3 that increasing the size of the mask provides SDI with more potential solutions to integrating prompt instructions into the image context, resulting in outputs that more closely follow the instruction. Finally, in Sec. 3.4, we test the hypotheses that interpret the internal mechanics of the SDI model, with a particular focus on the relationship between the inpainting conditioning and the cross-attention layer. The analysis of the SDI model helps us understand the factors leading to successful instruction-following inpainting.

### 3.1. Stable Diffusion Inpainting Model (SDI)

The SDI model receives a prompt  $p$ , an image  $I \in \mathbb{R}^{H \times W \times 3}$ , and a mask  $M \in \mathbb{R}^{H \times W}$  that specifies the inpainting area. To prevent the model from copying content

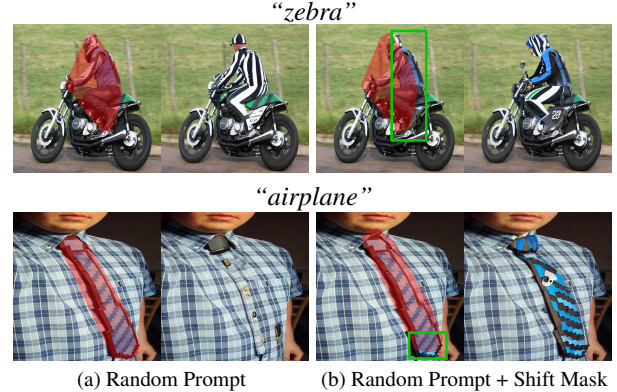


Figure 3. Visualization of contextual influence: A random prompt, unrelated to the image condition, is assigned. The input mask is shown in columns 1 and 3, along with the corresponding prompt, while shifted areas are highlighted with a green frame. The resulting outputs are displayed in columns 2 and 4.

directly from  $I$ , the masked area of  $I$  is set to zero, yielding  $I^c = (1 - M) \odot I$ . Since the UNet operates in VAE [14] latent space,  $I^c$  is encoded as the image condition  $z^c = \mathcal{E}(I^c) \in \mathbb{R}^{(H/4) \times (W/4) \times 4}$  and  $\mathcal{E}$  denotes the pretrained VAE encoder. To match the input size, the SDI model uses an interpolated mask condition  $M^c \in \mathbb{R}^{(H/4) \times (W/4)}$ , created by downsampling  $M$  with nearest-neighbor interpolation. The final inpainting noise prediction from the diffusion model is  $\epsilon_\theta(z_t, z^c, M^c, t, p)$ , where  $\epsilon_\theta$  represents the SDI UNet model,  $z_t$  is the noise latent at timestep  $t \in [0, T]$ , and initial noise  $z_T$  is sampled from  $\mathcal{N}(\mathbf{0}, \mathbf{I})$ . To control the influence of prompt  $p$ , we follow classifier-free guidance (CFG) [9], modifying the noise prediction with a scaling parameter  $w \in \mathbb{R}$ :

$$\begin{aligned} \hat{\epsilon}_\theta(z_t, z^c, M^c, t, p) &= \epsilon_\theta(z_t, z^c, M^c, t, \emptyset) \\ &+ w(\epsilon_\theta(z_t, z^c, M^c, t, p) - \epsilon_\theta(z_t, z^c, M^c, t, \emptyset)) \end{aligned} \quad (1)$$

To evaluate the inpainting results in our study, we use a set of six metrics adopted from BrushBench [13]. These metrics cover three key areas: **Image Quality**, measured by Image Reward (IR) [32], HPS [30], and Aesthetic Score (AS) [27]; **Background Preservation**, assessed using PSNR and LPIPS[40]; and **Instruction Following**, evaluated through CLIP [24]. Additionally, we introduce a novel Intersection-over-Union (IoU) score to specifically capture the mask-fitting quality, complementing the CLIP Score by distinguishing mask accuracy from prompt-adherence. This score is computed by the IoU between input mask and auto-labeled mask via SAM [15], as detailed in Sec. 7.3.

### 3.2. Influence of Image Condition $z^c$

The random masking strategy of SDI is via creating masked data by randomly masking 25% of image areas in LAION-

	AS	LPIPS	CLIP <sub>IN</sub>	CLIP <sub>GT</sub>
Original	5.89	0.04	18.66	18.66
Shift Mask	5.89	0.04	18.61	18.61
Random Prompt	5.79	0.04	15.57	15.62
Random + Shift	5.66	0.03	15.09	16.38

Table 1. Table of SDI model on different settings toward inpainting COCO dataset. CLIP<sub>IN</sub> denotes the CLIP similarity toward the input prompt, while CLIP<sub>GT</sub> for the ground truth prompt.

5B [27], aiming to enhance generalizability across various inputs. To investigate the mask distribution under this random strategy, we define three mask placements: “not masked,” “partially masked,” and “fully masked.” Although the exact SDI training mask distribution is not accessible, our analysis on the COCO dataset as a surrogate reveals that, with a 25% mask coverage, over 80% of training data falls under the “not masked” or “partially masked” categories (see Sec. 8.1 in the Appendix for details). Thus, we hypothesize that **the random masking design optimizes SDI for maintaining overall image harmony rather than strict prompt-adherence**. For instance, in the second row of Fig. 3a, when prompted with “airplane” instead of the actual ground-truth “tie”, SDI ignores the prompt and generates contextually consistent but unrelated content.

To validate this, we select 600 mask and ground-truth pairs from COCO [16]. In the “random prompt” setting, ground truth prompts are replaced with random ones. Results in Tab. 1 show that the CLIP score for ground truth prompts (CLIP<sub>GT</sub>) closely matches that for input prompts (CLIP<sub>IN</sub>), indicating that SDI favors contextual coherence over strict prompt-adherence. For example, in Fig. 3a, SDI interprets contextual hints by generating an object riding on a motorcycle rather than a zebra as prompted, producing a person with zebra-patterned clothing instead. In the “random prompt + shifted mask” setting, we shift the mask by 25 pixels to add more ground-truth information into the image condition  $z^c$ . This adjustment decreases instruction-following accuracy, reflected by a 3% drop in CLIP<sub>IN</sub> and a 5% increase in CLIP<sub>GT</sub> compared to the “random prompt” case. In Fig. 3b, when an object, like a person or tie, is visible in  $z^c$ , SDI can revert the whole object. This analysis confirms that **the context provided by  $z^c$  significantly limits SDI’s instruction following**.

### 3.3. Influence of Input Mask $M$

In the preceding analysis, we observe that the inpainting result can be hugely guided by the image condition  $z^c$ , leading to its deficiency in the instruction following. Here, we explore how to adjust the input mask  $M$  to promote instruction-following outputs across varied inputs. Studying the SDI model under complex scenarios—such as multiple or rough masks, unrelated prompt instruction  $p$  for

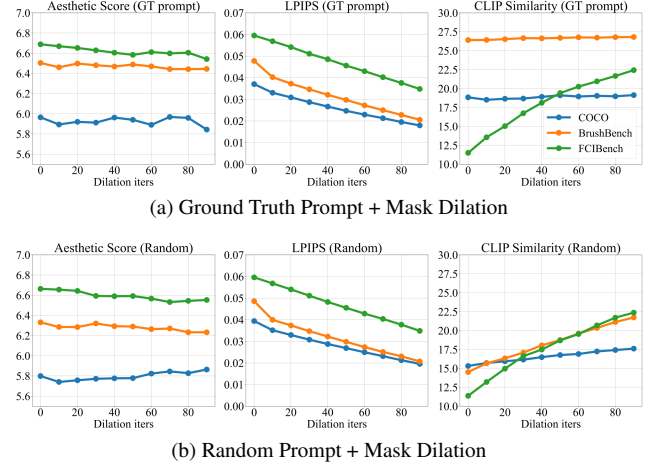


Figure 4. Illustration of mask size impact on inpainting metrics.

reference image  $I$ —requires a more comprehensive benchmark. However, since the COCO dataset includes only the precise masks, and its prompts for generating are simple and highly related to the image context, we propose FCIBench, which incorporates rough masks, multi-mask, and complex prompts with unrelated contexts of image condition. FCIBench compensates the shortage of existing benchmarks [13, 16], as shown in Sec. 7.

Building on our observation in the first row of Fig. 3a that the prompt “zebra” and ground-truth “person” coexist, we explore which modifications to the input mask  $M$  can facilitate this coexistence across different scenarios. Intuitively, we hypothesize that **increasing the mask size may provide SDI with more potential solutions to integrate prompt instructions into the image context, rather than simply disregarding the prompt**. The results, illustrated in Fig. 4, reveal that in both scenarios, AS remains nearly constant, indicating that image quality is nearly invariant to mask size. Additionally, LPIPS decrease as the non-masked area became smaller. Finally, as mask size increases, CLIP consistently improves, especially in Fig. 4b where the prompt was unrelated to the background context. This finding supports our hypothesis that **increasing the mask size can enhance prompt-adherence in the model’s output**.

### 3.4. The Mechanism Behind Inpainting

In Sec. 3.2, we identify that SDI’s deficiency in instruction-following stems from its preference for maintaining harmony within the image context. Although in Sec. 3.3 we show that simply enlarging the mask  $M$  can better balance instruction-following and contextual harmony, this solution is impractical, as we seek to modify only specific regions within the given mask. This discussion raises two key questions: (1) **How does the image condition influence features within the masked area?** and (2) **How does prompt information selectively affect only the masked area?** By

"A golden retriever wearing astronaut gear, in cyberpunk style"

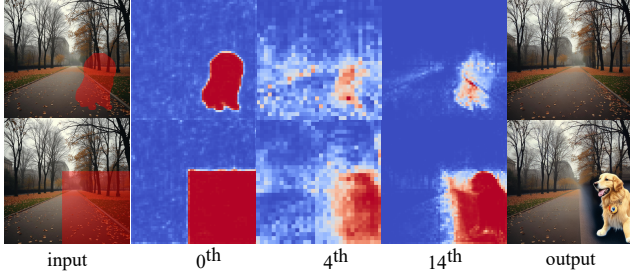


Figure 5. A self-attention visualization in different layers. The attention from  $M$  is colored.

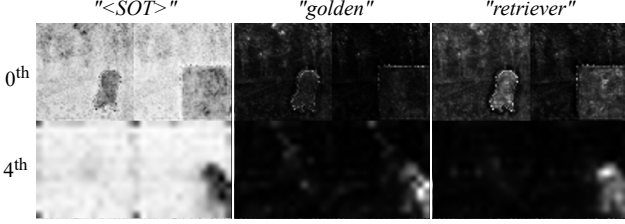


Figure 6. A cross-attention visualization of Fig. 5 in different cross-attention layers. The attention follows the input mask shape in the first layer, adapting to the output shape in the deeper layer.

uncovering the underlying mechanisms behind these questions, we can explore ways to refine SDI’s learned behavior.

Our initial hypothesis to the first question is that **features within the masked area become progressively diluted by background elements during down-sampling and self-attention operations**. This is illustrated in Fig. 5, where we compared two cases, “precise mask” (row 1) and “large rough mask” (row 2). For both cases, the mask shape is clearly visible in early layers. However, in the subsequent layers (4th, 14th) of the first case, attention within the masked area becomes further diluted by background elements. This results in the final image output with background-like elements in the masked area that are totally unrelated to the prompt. By contrast, in case 2, the attention of the generated object within the masked area successfully deviates from the background elements, aligning closely with the generated object. This results in a more instruction-following outcome, supporting our hypothesis.

To address the second question, we hypothesize that, given the architecture of SDI, **certain channels within the cross-attention key are highly adapted to the mask input, selectively enhance prompt response toward the masked region**. This adaptation is illustrated in Fig. 6 and is supported by the classifier-free guidance differences observed in Sec. 9. To strengthen this hypothesis, we measure the numerical influence made by input  $M$ . As we mentioned in Sec. 3.1, the mask input  $M$  is processed into  $M^c$  and  $z^c$ . In the initial input layer of UNet, these inputs are Concatenated and forwarded into  $h_0$  =

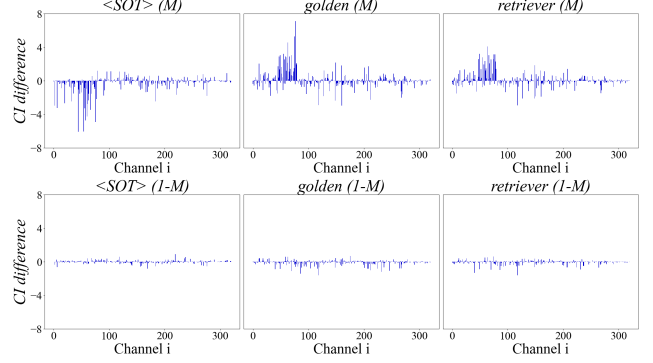


Figure 7. An illustration of the difference of channel influence indicator ( $\Delta CI$ ) across different channels, in the region  $M$  (first row) and the region  $(1 - M)$  (second row).

$\Phi_0(\text{Concat}([z_t, M^c, z^c])) \in \mathbb{R}^{(H/4) \times (W/4) \times 320}$ , where  $\Phi_0$  is the first convolutional layer of the denoising UNet. Following this, the cross-attention layer projects  $h_0$  feature into the query representation  $Q = W_Q h_0$ , where  $Q \in \mathbb{R}^{(H/4 \times W/4) \times 320}$ . Simultaneously, the prompt embedding  $p$  is projected into  $K = W_K \Psi(p)$ ,  $V = W_V \Psi(p)$ , where  $\Psi$  is the CLIP text encoder and  $K, V \in \mathbb{R}^{77 \times 320}$ . The cross-attention output is then computed as  $\text{Attention}(Q, K, V) = \text{Softmax}(QK^T / \sqrt{d})V$ .

To test our assumption that specific channels of query  $Q$  are highly adapted to the given key token  $k \in \mathbb{R}^{320}$  in certain feature channels, we define a Channel Influence Indicator ( $CI$ ) here:

$$CI(Q, M, k, i) = \frac{1}{\sum_j \bar{M}_j} \sum_{j=1}^{H \times W / 16} (Q_j \odot k)_i \cdot \bar{M}_j, \quad (2)$$

where  $\odot$  denotes the Hadamard product, the subscript  $i$  refers to the  $i$ -th element of a vector, and  $\bar{M}$  represents the flattened version of  $M$ . Since the sum of  $CI$  across different channels is positively correlated with the  $QK^T$  computation in cross-attention, the  $CI$  indicator offers a means to visualize the influence introduced by  $M$  within specific feature channels.

To measure the difference leading by mask input  $M$ , we choose the input mask of the second row of Fig. 5, denoted as  $M^l$ , compared with the zero matrix  $M^n$ . We then define  $Q^l = W_Q \Phi_0(\text{Concat}([z_t, M^l, z^l]))$  and  $Q^n = W_Q \Phi_0(\text{Concat}([z_t, M^n, z^n]))$ , where  $z^l$  is the image condition given  $M^l$ , similarly the  $z^n$  and  $M^n$ .

To demonstrate that mask input ( $M^l$  in this case) significantly influences  $QK^T$  computations in certain channels of given masked area  $M^l$ , we plot  $\Delta CI = CI(Q^l, M^l, k, i) - CI(Q^n, M^l, k, i)$ , at initial timestep  $t=T$ , where both  $Q^l$  and  $Q^n$  share the same noise latent  $z_t$ . In Fig. 7, we observe that the  $\Delta CI$  shifts more markedly within  $M^l$  area than in  $(1 - M^l)$  area. For non-informative tokens (i.e. “<SOT>”),  $\Delta CI$  decreases significantly, leading to a relative increase

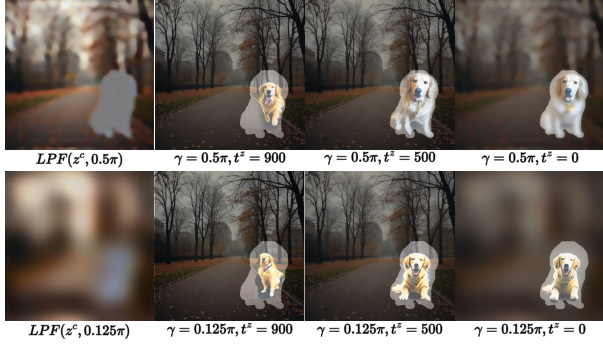


Figure 8. A illustration of the  $z^{fc}$  (column 1) and the output leading by different values of  $t^z$  (columns 2,3, and 4). The input mask is highlighted by overlaying it onto the output images.

in attention toward other informative tokens. For meaningful tokens such as “golden” and “retriever”,  $\Delta CI$  increases, especially within the first 80 channels. This finding supports our hypothesis that **cross-attention key features adapt specifically to mask input, particularly in the first 80 channels, enabling selective prompt influence within  $M$** . More evaluations can be found in Sec. 9.4.

## 4. Method

In Sec. 3.2, we identify that the image context provided by  $z^c$  can impede instruction-following in the SDI model. In Sec. 3.3 and Sec. 3.4, we observe that the  $M^c$  plays an important role in the cross-attention layer, the inclusion of  $M^c$  leading to prompt-adherence by shifting the cross-attention features. Building on these insights, we propose FreeCond to directly reduce the heavy reliance on the image context provided by  $z^c$  and increase the feature shift led by  $M^c$ . With FreeCond, we can achieve improved instruction-following for the SDI-based approach in a post-hoc manner without additional fine-tuning or computational costs.

### 4.1. FreeCond Image Condition

In light of the phenomenon observed in Sec. 3.2, where inpainting outputs can be significantly influenced or dominated by the image condition  $z^c$ , it appears reasonable to reduce the influence of  $z^c$  to improve instruction following. However, since the inpainting model relies on  $z^c$  to preserve the background, any adjustments to  $z^c$  can compromise the mask preservation. Nonetheless, based on the nature of the T2I diffusion process, as described in [2, 28, 35], we note that low-frequency components are formed in early steps while high-frequency details emerge in later steps. In other words, we can still largely preserve the background in the final output by inputting only the low-frequency portion of  $z^c$  in the early step and then transitioning to the original  $z^c$ .

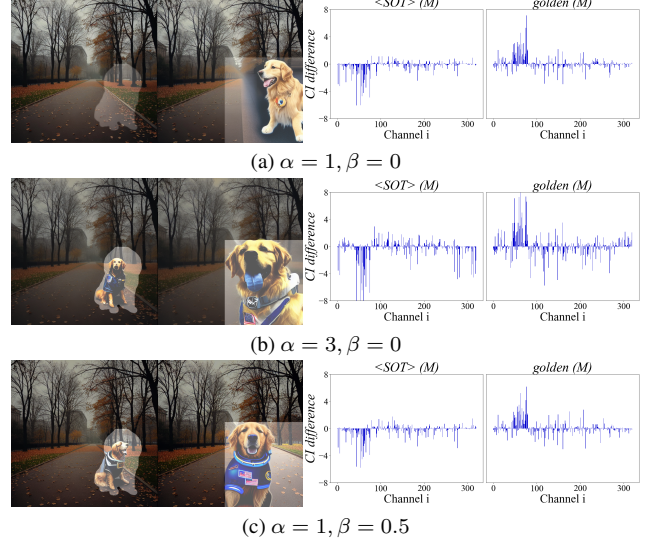


Figure 9. A illustration of the effect of  $M^{fc}$  and corresponding CI plot for “large mask” (columns 3 and 4). The input mask is highlighted by overlaying it onto the output images.

We define the FreeCond image condition as:

$$z^{fc} = \begin{cases} LPF(z^c, \gamma), & \text{if } t \geq t^{fc} \\ z^c, & \text{if } t < t^{fc} \end{cases} \quad (3)$$

where  $LPF(z^c, \gamma)$  is a low-pass filter that excludes high-frequency components above the threshold  $\gamma$ , and  $t^{fc}$  is the timestep control parameter, with lower values of  $t^{fc}$  producing a blurrier output. The effect of  $z^{fc}$  is demonstrated in Fig. 8. By modifying  $z^{fc}$  in the early step, such as setting  $t^{fc} \in [0.5T, 0.9T]$ , we can effectively improve instruction-following with minimal impact on background preservation. Since the  $LPF$  filters out high-frequency image information, the overall image context is disrupted, thus enhancing instruction-following by reducing interference from the original image context.

### 4.2. FreeCond Mask Condition

Building on our observations in Sec. 3.4, we find that the T2I inpainting effect of the SDI model is raised by the shifting in cross-attention features with non-zero mask input  $M$ . Further analysis in Sec. 9.4 reveals that while both  $z^c$  and  $M^c$  affect the inpainting outcome, shifts in cross-attention features are primarily driven by  $M^c$  values. Based on this, we explore the potential to enhance cross-attention feature shifts by manipulating the mask condition  $M^c$ . Accordingly, we introduce a FreeCond mask condition,  $M^{fc}$ , which scales up the value of  $M^c$  to induce a stronger cross-attention feature shift, thereby improving prompt alignment. Another observation, shown in Fig. 7, is that the CI indicator in the  $(1 - M)$  region is subtly impacted by the mask  $M$ . Thus, increasing mask values within

Methods	Image Quality			Background Preservation		Instruction Following	
	ImageReward↑	HPS ↑	Aesthetic↑	PSNR↑	LPIPS ↓	CLIP Score ↑	IoU Score↑
SDI [26]	-1.21/1.22/-1.95	0.24/0.27/0.17	<b>5.90</b> /6.50/ <b>6.69</b>	25.95/27.26/25.54	<b>0.04/0.04/0.06</b>	18.67/26.41/11.45	0.49/0.62/0.07
SDI <sup>fc</sup>	-1.23/1.14/-1.29	0.24/0.27/0.20	<b>5.86</b> / <b>6.54</b> /6.44	24.79/26.73/24.58	<b>0.04</b> /0.05/0.07	18.82/26.46/18.27	0.65/0.70/0.54
CNI [39]	-1.24/1.15/-1.95	0.24/0.27/0.17	5.78/6.44/6.63	<b>26.23</b> / <b>27.69</b> / <b>25.81</b>	<b>0.04/0.04/0.06</b>	18.83/26.04/11.38	0.57/0.60/0.12
CNI <sup>fc</sup>	-1.24/1.11/-1.52	0.24/0.27/0.19	5.76/6.46/6.49	25.58/27.06/25.23	<b>0.04</b> /0.05/0.07	19.10/25.97/16.01	0.67/0.67/0.45
HDP [20]	-1.19/1.18/-1.40	<b>0.25</b> /0.27/0.20	5.79/6.46/6.57	24.95/27.02/25.23	<b>0.04/0.05/0.06</b>	19.14/26.45/17.08	0.60/0.63/0.36
HDP <sup>fc</sup>	-1.27/1.20/-1.15	0.24/ <b>0.28</b> /0.20	5.75/6.52/6.43	23.63/26.00/23.48	0.05/0.05/0.08	19.17/26.41/19.37	0.77/0.68/0.67
PP [42]	-1.19/1.21/-1.13	0.22/0.27/0.19	5.79/6.30/6.40	25.63/27.62/25.29	0.05/0.05/0.07	18.74/27.02/19.05	0.59/0.55/0.43
PP <sup>fc</sup>	<b>-1.15</b> /1.20/-1.12	0.22/0.27/0.19	5.73/6.33/6.39	25.41/27.37/24.32	0.05/0.05/0.08	19.12/ <b>27.05</b> /19.43	0.67/0.59/0.52
BN [13]	-1.24/ <b>1.24</b> /-1.08	0.24/0.27/ <b>0.21</b>	5.77/6.53/6.38	24.89/26.37/24.35	0.05/0.06/0.07	19.22/26.50/19.96	0.83/ <b>0.75</b> /0.77
BN <sup>fc</sup>	-1.31/1.21/ <b>-1.05</b>	0.23/0.27/ <b>0.21</b>	5.77/6.53/6.43	24.21/25.38/23.49	0.05/0.06/0.08	<b>19.27</b> /26.50/ <b>20.18</b>	<b>0.85/0.75/0.78</b>
SDXL [23]	-1.06/1.32/-1.72	0.25/0.29/0.19	5.74/6.40/6.55	24.61/25.78/25.00	0.03/0.03/0.04	19.09/26.96/14.16	0.53/0.68/0.09
SDXL <sup>fc</sup>	-0.94/1.30/-0.78	0.25/0.29/0.22	5.69/6.34/6.56	24.15/26.12/24.59	0.04/0.04/0.05	19.77/27.16/22.36	0.60/0.64/0.44

Table 2. Quantitative results showing improvements achieved by FreeCond (denoted with <sup>fc</sup>) across three benchmarks: **COCO**, **BrushBench**, and **FCIBench**, separated by “/” respectively. Note: we discovered that the BrushBench results reported in [13] were calculated with an NSFW detector; as NSFW detection may vary, we disable it here to ensure a more precise evaluation.

the  $(1 - M)$  region can amplify feature shifts within  $M$ . To test this, we define the FreeCond mask condition:

$$M^{fc} = \alpha \cdot M^c + \beta \cdot (1 - M^c) \quad (4)$$

where  $\alpha$  and  $\beta$  are scaling factors to control the influence of  $M^c$  and  $(1 - M^c)$ . The impact of  $M^{fc}$  is illustrated in Fig. 9. Compared to the baseline results in Fig. 9a, the output with a  $M^{fc}$  exhibits greater prompt-adherence. For instance, in the “precise mask” condition, instead of filling the background element, the “golden retriever wearing an astronaut gear” appears. Additionally, in the “large mask” setting, the golden retriever now includes the “astronaut gear”. We also provide the response of the CI indicator for  $M^{fc}$  in the right side of Fig. 9 to show that modifying the latent mask  $M^c$  can effectively enhance feature shifts within the cross-attention layer.

With our proposed alteration, the noise prediction function from Eq. (1) can be generalized as  $\hat{\epsilon}_\theta(z_t, z^{fc}, M^{fc}, t, p)$ . As FreeCond only modifies the input, it is compatible with other SDI-based models, detailed in Sec. 10.

## 5. Experiment

### 5.1. Experiment Setting

We conduct experiments on three datasets: COCO [16], BrushBench [13], and our proposed FCIBench, each comprising 600 instruction pairs (details in Sec. 7). To account for the inherent differences between the baseline methods, we provide the specific hyperparameter settings and further discussion in Sec. 11. The computational metrics used for evaluation are detailed in Sec. 3.1.

## 5.2. Experiment Results

Tab. 2 presents the quantitative improvements achieved with the inclusion of FreeCond. We compare FreeCond with the original SDI [26] and its variants, including ControlNet In-painting (CNI) [39], HD-Painter (HDP) [20], PowerPaint (PP) [42], and BrushNet (BN) [13]. Additionally, we assess SDXL [23], a much larger model, as a reference to showcase the zero-shot improvements by FreeCond, it is not directly compared with other baselines.

In our proposed FCIBench, shown in the right section of each block. Designed as a more challenging benchmark, FreeCond demonstrates substantial gains, achieving a 60% increase over the original SDI model and a 1% improvement over BrushNet, the existing SOTA. Additionally, FreeCond improves metrics such as IR, HPS, and IoU across all baselines. Notably, both BrushNet and PowerPaint benefit from FreeCond with modest increases in IoU yet larger gains in CLIP score, highlighting FreeCond’s capability to further enhance prompt-adherence in SOTA methods that are optimized for mask-fitting. For the two widely used datasets, COCO and BrushBench—represented in the left and middle sections of each block—current inpainting methods demonstrate similar performance levels. FreeCond advances this upper limit, increasing BrushNet’s CLIP score from 19.22 to 19.27 on COCO and PowerPaint’s CLIP score from 27.02 to 27.05 on BrushBench. Overall, FreeCond enhances performance across both instruction following and image quality, with improvements in IR, HPS, and CLIP scores.

Nevertheless, modifying learned mechanism with FreeCond can lead to minor degradations in detail-oriented metrics, such as AS, PSNR, and LPIPS. These minor distortions, are generally imperceptible to human preference, as evidenced by the increases in the human-preference-based

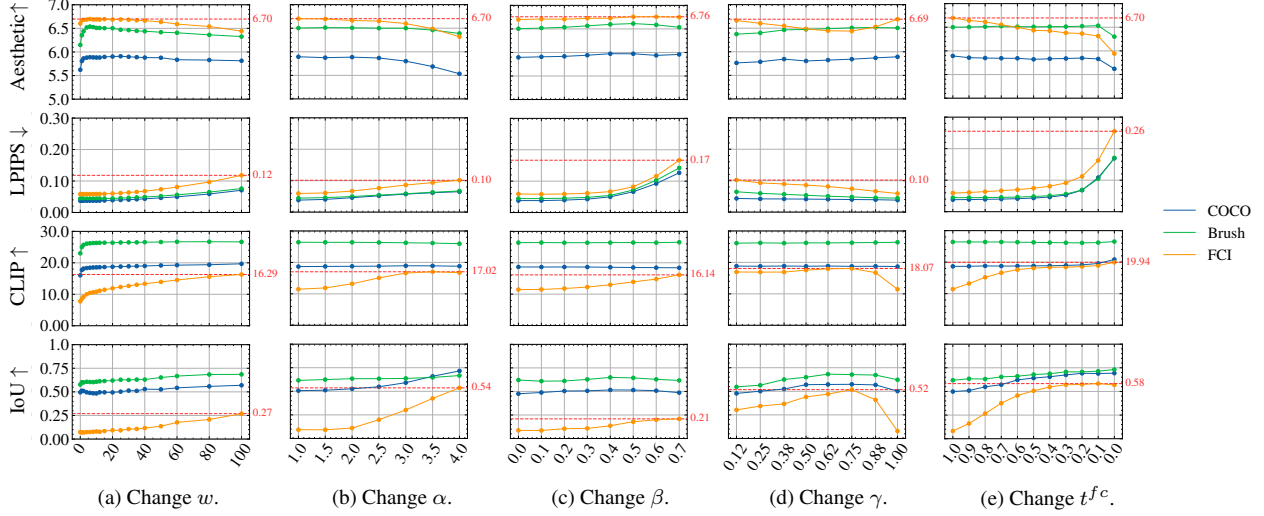


Figure 10. Illustration of the influence of CFG ( $w$ ) and each hyperparameter of FreeCond( $\alpha, \beta, \gamma, t^{fc}$ ), highest values are denoted.



Figure 11. The qualitative illustration of Fig. 10, the change compared to normal SDI is colored.

metrics IR and HPS. These results are more apparent in the qualitative results, discussed further in Sec. 11.

### 5.3. Ablation Study

In Fig. 10 and Fig. 11, we examine the impact of adjusting five components: (a) the classifier-free guidance (CFG) scale  $w$  [9], (b) the inner-mask scale  $\alpha$ , (c) the outer-mask scale  $\beta$ , (d) the LPF threshold  $\gamma$  with a fixed  $t^{fc} = 25$ , and (e) the LPF timestep  $t^{fc}$  with  $\gamma = 0.75\pi$ . For each test, we fix the parameters at  $(w, \alpha, \beta, \gamma, t^{fc}) = (15, 1, 0, \pi, T)$  (the default configuration of original SDI) and vary only one parameter at a time. Based on quantitative and qualitative outcomes, we summarize our findings below.

**Effect of  $w$ .** As discussed in Sec. 3.2, SDI’s random masking strategy prioritizes generating objects within the mask rather than strict mask conformity. Therefore, increasing  $w$  in Fig. 11a primarily enhances prompt-related details without substantially increasing object size. This outcome is further reflected in the **lesser improvement of the IoU score compared to the CLIP score** in Fig. 10a.

**Effect of  $\alpha$ .** As explained in Sec. 4, increasing  $\alpha$  intensifies the cross-attention response within the masked area, **enhancing both prompt-adherence and mask-fitting**, as illustrated in Fig. 11b and Fig. 9b. However, excessively

high  $\alpha$  disrupts the learned feature distribution, leading to over-saturated results and a drop in AS.

**Effect of  $\beta$ .** Unlike other parameters, increasing  $\beta$  **enhances both the CLIP score and AS**, indicating a stronger self-attention interaction between  $M$  and  $1 - M$ , which results in a more harmonious output. However, as shown in Fig. 11c and Fig. 9c, higher  $\beta$  values also increase background distortion, reflected by the LPIPS in Fig. 10c.

**Effect of  $z^{fc}$  (controlled by  $\gamma$  and  $t^{fc}$ ).** These parameters control the frequency components of  $z^{fc}$ , which play a key role in reducing contextual influence and establishing prompt-related structures at early timesteps. As shown in Fig. 10e, increasing  $t^{fc}$  significantly **improves both CLIP and IoU scores**. This is reflected in Fig. 11d, where mask-fitting is improved while prompt-adherence is lacking (e.g., the “moss and flowers” are not fully generated).

## 6. Conclusion

In this work, we identify an instruction-following deficiency that persists across current SDI-based inpainting methods, particularly when complex prompts are provided alongside unrelated image conditions. Through an in-depth investigation of the SDI mechanism, we discover that its

selective inpainting capability within masked areas stems from a feature shift in the cross-attention layer. Based on this insight, we propose FreeCond—a training-free plug-in that introduces no additional computation overhead. Unlike classifier-free guidance, FreeCond enhances not only prompt-adherence but also mask-fitting and image quality. However, excessive parameter adjustments can degrade image quality, highlighting the need for careful tuning.

## References

- [1] Omri Avrahami, Ohad Fried, and Dani Lischinski. Blended latent diffusion. *ACM Transactions on Graphics*, 42(4):1–11, 2023. 3
- [2] Yogesh Balaji, Seungjun Nah, Xun Huang, Arash Vahdat, Jiaming Song, Qinsheng Zhang, Karsten Kreis, Miika Aittala, Timo Aila, Samuli Laine, et al. ediff-i: Text-to-image diffusion models with an ensemble of expert denoisers. *arXiv preprint arXiv:2211.01324*, 2022. 6
- [3] Mingdeng Cao, Xintao Wang, Zhongang Qi, Ying Shan, Xiaohu Qie, and Yinqiang Zheng. Masactrl: Tuning-free mutual self-attention control for consistent image synthesis and editing. In *Proceedings of the IEEE/CVF International Conference on Computer Vision*, pages 22560–22570, 2023. 3
- [4] Huiwen Chang, Han Zhang, Lu Jiang, Ce Liu, and William T Freeman. Maskgit: Masked generative image transformer. In *Proceedings of the IEEE/CVF Conference on Computer Vision and Pattern Recognition*, pages 11315–11325, 2022. 3
- [5] Chieh-Yun Chen, Li-Wu Tsao, Chiang Tseng, and Hong-Han Shuai. A cat is a cat (not a dog!): Unraveling information mix-ups in text-to-image encoders through causal analysis and embedding optimization. *arXiv preprint arXiv:2410.00321*, 2024. 3, 2
- [6] Jiwoo Chung, Sangeek Hyun, and Jae-Pil Heo. Style injection in diffusion: A training-free approach for adapting large-scale diffusion models for style transfer. In *Proceedings of the IEEE/CVF Conference on Computer Vision and Pattern Recognition*, pages 8795–8805, 2024.
- [7] Yingying Deng, Xiangyu He, Fan Tang, and Weiming Dong. Z\*: Zero-shot style transfer via attention reweighting. In *Proceedings of the IEEE/CVF Conference on Computer Vision and Pattern Recognition*, pages 6934–6944, 2024.
- [8] Amir Hertz, Ron Mokady, Jay Tenenbaum, Kfir Aberman, Yael Pritch, and Daniel Cohen-Or. Prompt-to-prompt image editing with cross attention control. *arXiv preprint arXiv:2208.01626*, 2022. 3
- [9] Jonathan Ho and Tim Salimans. Classifier-free diffusion guidance. *arXiv preprint arXiv:2207.12598*, 2022. 2, 3, 8
- [10] Teng-Fang Hsiao, Bo-Kai Ruan, and Hong-Han Shuai. Training-and-prompt-free general painterly harmonization using image-wise attention sharing. *arXiv preprint arXiv:2404.12900*, 2024. 3
- [11] Inbar Huberman-Spiegelglas, Vladimir Kulikov, and Tomer Michaeli. An edit friendly ddpm noise space: Inversion and manipulations. In *Proceedings of the IEEE/CVF Conference on Computer Vision and Pattern Recognition*, pages 12469–12478, 2024. 3
- [12] Changho Jo, Woobin Im, and Sung-Eui Yoon. In-n-out: Towards good initialization for inpainting and outpainting. *arXiv preprint arXiv:2106.13953*, 2021. 3
- [13] Xuan Ju, Xian Liu, Xintao Wang, Yuxuan Bian, Ying Shan, and Qiang Xu. Brushnet: A plug-and-play image inpainting model with decomposed dual-branch diffusion. *arXiv preprint arXiv:2403.06976*, 2024. 2, 3, 4, 7, 1
- [14] Diederik P Kingma. Auto-encoding variational bayes. *arXiv preprint arXiv:1312.6114*, 2013. 3
- [15] Alexander Kirillov, Eric Mintun, Nikhila Ravi, Hanzi Mao, Chloe Rolland, Laura Gustafson, Tete Xiao, Spencer Whitehead, Alexander C Berg, Wan-Yen Lo, et al. Segment anything. In *Proceedings of the IEEE/CVF International Conference on Computer Vision*, pages 4015–4026, 2023. 3
- [16] Tsung-Yi Lin, Michael Maire, Serge Belongie, James Hays, Pietro Perona, Deva Ramanan, Piotr Dollár, and C Lawrence Zitnick. Microsoft coco: Common objects in context. In *European Conference on Computer Vision*, pages 740–755. Springer, 2014. 2, 4, 7, 1, 3
- [17] Nan Liu, Shuang Li, Yilun Du, Antonio Torralba, and Joshua B Tenenbaum. Compositional visual generation with composable diffusion models. In *European Conference on Computer Vision*, pages 423–439. Springer, 2022. 3
- [18] Andreas Lugmayr, Martin Danelljan, Andres Romero, Fisher Yu, Radu Timofte, and Luc Van Gool. Repaint: Inpainting using denoising diffusion probabilistic models. In *Proceedings of the IEEE/CVF Conference on Computer Vision and Pattern Recognition*, pages 11461–11471, 2022. 3
- [19] Yang Luo, Yiheng Zhang, Zhaofan Qiu, Ting Yao, Zheneng Chen, Yu-Gang Jiang, and Tao Mei. Freeenhance: Tuning-free image enhancement via content-consistent noising-and-denoising process. In *Proceedings of the 32nd ACM International Conference on Multimedia*, pages 7075–7084, 2024. 3
- [20] Hayk Manukyan, Andranik Sargsyan, Barsegh Atanyan, Zhangyang Wang, Shant Navasardyan, and Humphrey Shi. Hd-painter: high-resolution and prompt-faithful text-guided image inpainting with diffusion models. *arXiv preprint arXiv:2312.14091*, 2023. 2, 3, 7, 1, 4, 6
- [21] Chenlin Meng, Yutong He, Yang Song, Jiaming Song, Jianjun Wu, Jun-Yan Zhu, and Stefano Ermon. Sredit: Guided image synthesis and editing with stochastic differential equations. *arXiv preprint arXiv:2108.01073*, 2021. 3
- [22] Jialun Peng, Dong Liu, Songcen Xu, and Houqiang Li. Generating diverse structure for image inpainting with hierarchical vq-vae. In *Proceedings of the IEEE/CVF Conference on Computer Vision and Pattern Recognition*, pages 10775–10784, 2021. 3
- [23] Dustin Podell, Zion English, Kyle Lacey, Andreas Blattmann, Tim Dockhorn, Jonas Müller, Joe Penna, and Robin Rombach. Sdxl: Improving latent diffusion models for high-resolution image synthesis. *arXiv preprint arXiv:2307.01952*, 2023. 2, 7, 4, 6
- [24] Alec Radford, Jong Wook Kim, Chris Hallacy, Aditya Ramesh, Gabriel Goh, Sandhini Agarwal, Girish Sastry, Amanda Askell, Pamela Mishkin, Jack Clark, et al. Learning transferable visual models from natural language super-

- vision. In *International Conference on Machine Learning*, pages 8748–8763. PMLR, 2021. 2, 3
- [25] Aditya Ramesh, Mikhail Pavlov, Gabriel Goh, Scott Gray, Chelsea Voss, Alec Radford, Mark Chen, and Ilya Sutskever. Zero-shot text-to-image generation. In *International Conference on Machine Learning*, pages 8821–8831. Pmlr, 2021. 3
- [26] Robin Rombach, Andreas Blattmann, Dominik Lorenz, Patrick Esser, and Björn Ommer. High-resolution image synthesis with latent diffusion models. In *Proceedings of the IEEE/CVF Conference on Computer Vision and Pattern Recognition*, pages 10684–10695, 2022. 1, 3, 7, 4
- [27] Christoph Schuhmann, Romain Beaumont, Richard Vencu, Cade Gordon, Ross Wightman, Mehdi Cherti, Theo Coombes, Aarush Katta, Clayton Mullis, Mitchell Wortsman, et al. Laion-5b: An open large-scale dataset for training next generation image-text models. *Advances in Neural Information Processing Systems*, 35:25278–25294, 2022. 3, 4
- [28] Chenyang Si, Ziqi Huang, Yuming Jiang, and Ziwei Liu. Freeu: Free lunch in diffusion u-net. In *Proceedings of the IEEE/CVF Conference on Computer Vision and Pattern Recognition*, pages 4733–4743, 2024. 3, 6
- [29] Su Wang, Chitwan Saharia, Ceslee Montgomery, Jordi Pont-Tuset, Shai Noy, Stefano Pellegrini, Yasumasa Onoe, Sarah Laszlo, David J Fleet, Radu Soricut, et al. Imagen editor and editbench: Advancing and evaluating text-guided image inpainting. In *Proceedings of the IEEE/CVF Conference on Computer Vision and Pattern Recognition*, pages 18359–18369, 2023. 3
- [30] Xiaoshi Wu, Keqiang Sun, Feng Zhu, Rui Zhao, and Hongsheng Li. Human preference score: Better aligning text-to-image models with human preference. In *Proceedings of the IEEE/CVF International Conference on Computer Vision*, pages 2096–2105, 2023. 3
- [31] Shaoan Xie, Zhifei Zhang, Zhe Lin, Tobias Hinz, and Kun Zhang. Smartbrush: Text and shape guided object inpainting with diffusion model. In *Proceedings of the IEEE/CVF Conference on Computer Vision and Pattern Recognition*, pages 22428–22437, 2023. 3, 1, 7
- [32] Jiazheng Xu, Xiao Liu, Yuchen Wu, Yuxuan Tong, Qinkai Li, Ming Ding, Jie Tang, and Yuxiao Dong. Imagereward: Learning and evaluating human preferences for text-to-image generation. *Advances in Neural Information Processing Systems*, 36, 2024. 3
- [33] Shiyuan Yang, Xiaodong Chen, and Jing Liao. Uni-paint: A unified framework for multimodal image inpainting with pretrained diffusion model. In *Proceedings of the 31st ACM International Conference on Multimedia*, pages 3190–3199, 2023. 3
- [34] Mingyang Yi, Aoxue Li, Yi Xin, and Zhenguo Li. Towards understanding the working mechanism of text-to-image diffusion model. *arXiv preprint arXiv:2405.15330*, 2024. 3
- [35] Mingyang Yi, Aoxue Li, Yi Xin, and Zhenguo Li. Towards understanding the working mechanism of text-to-image diffusion model. *arXiv preprint arXiv:2405.15330*, 2024. 3, 6
- [36] Jiahui Yu, Zhe Lin, Jimei Yang, Xiaohui Shen, Xin Lu, and Thomas S Huang. Generative image inpainting with contextual attention. In *Proceedings of the IEEE/CVF Conference on Computer Vision and Pattern Recognition*, pages 5505–5514, 2018. 3
- [37] Jiahui Yu, Zhe Lin, Jimei Yang, Xiaohui Shen, Xin Lu, and Thomas S Huang. Free-form image inpainting with gated convolution. In *Proceedings of the IEEE/CVF International Conference on Computer Vision*, pages 4471–4480, 2019.
- [38] Yanhong Zeng, Jianlong Fu, Hongyang Chao, and Baineng Guo. Aggregated contextual transformations for high-resolution image inpainting. *IEEE Transactions on Visualization and Computer Graphics*, 29(7):3266–3280, 2022. 3
- [39] Lvmin Zhang, Anyi Rao, and Maneesh Agrawala. Adding conditional control to text-to-image diffusion models. In *Proceedings of the IEEE/CVF International Conference on Computer Vision*, pages 3836–3847, 2023. 2, 3, 7, 4
- [40] Richard Zhang, Phillip Isola, Alexei A Efros, Eli Shechtman, and Oliver Wang. The unreasonable effectiveness of deep features as a perceptual metric. In *Proceedings of the IEEE/CVF Conference on Computer Vision and Pattern Recognition*, pages 586–595, 2018. 3
- [41] Chuanxia Zheng, Tat-Jen Cham, and Jianfei Cai. Pluralistic image completion. In *Proceedings of the IEEE/CVF Conference on Computer Vision and Pattern Recognition*, pages 1438–1447, 2019. 3
- [42] Junhao Zhuang, Yanhong Zeng, Wenran Liu, Chun Yuan, and Kai Chen. A task is worth one word: Learning with task prompts for high-quality versatile image inpainting. *arXiv preprint arXiv:2312.03594*, 2023. 2, 3, 7, 1, 4, 6

# FreeCond: Free Lunch in the Input Conditions of Text-Guided Inpainting

## Supplementary Material

### 7. Benchmark

#### 7.1. FreeCondInpainting Benchmark

##### 7.1.1. Goal

The goal of FCIBench is to facilitate the evaluation of text-guided image inpainting in diverse, user-oriented scenarios. Previous text-guided inpainting methods primarily focus on replacing objects based on user-specific instructions, such as altering a person's hair color or refining artifacts in input images (*e.g.*, restoring damaged areas). However, modern text-to-image (T2I) editing often requires generating entirely new objects or scenes from scratch. For instance, as shown in the third row of Fig. 13, FCIBench introduces tasks like creating *penguins*, *motorcycles*, or *fluttering paper cranes* in empty spaces.

##### 7.1.2. Data collection

FCIBench consists of 110 creative prompts, 600 background images, and 600 human-labeled masks.

**Prompt generation.** The prompts are generated using ChatGPT-4, following a structured template:

*[an object], [detailed description], [in some style]*

For example:

- A glass teapot filled with colorful floating islands, in surrealist style.
- A human fighting a huge dinosaur, pixel art style.

**Background images.** Unlike existing benchmarks that primarily use human-created images, FCIBench leverages state-of-the-art (SOTA) T2I models, including DALLE, SD3, and Flux, to generate high-quality background images. These models not only produce visually stunning results but also provide high-resolution outputs ( $1024 \times 1024$ ), which are beneficial for future research. The background images are generated using GPT with a specific template:

*empty space, [detailed description], [in some style]*

For example:

- empty space, futuristic space station interior with panoramic windows overlooking a planet, sci-fi style.
- empty space, alien jungle with twisted flora and luminous fungi, extraterrestrial style.

**Mask.** First, we generate the corresponding object using the input prompt via SD3. This approach allows us to label the object directly from the generated result, as illustrated in Fig. 12. Subsequently, we randomly pair the annotated mask with a different background image.

#### 7.2. Comparison of Datasets

The comparison can be found in Fig. 13 and Tab. 3.

"A human fighting a huge dinosaur, pixel art style"

SD3



Labeled Mask

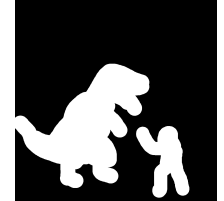


Figure 12. An illustration of the mask annotation process. Instead of auto-segmentation tool, we adopt human labeling to mimic real-world usages.

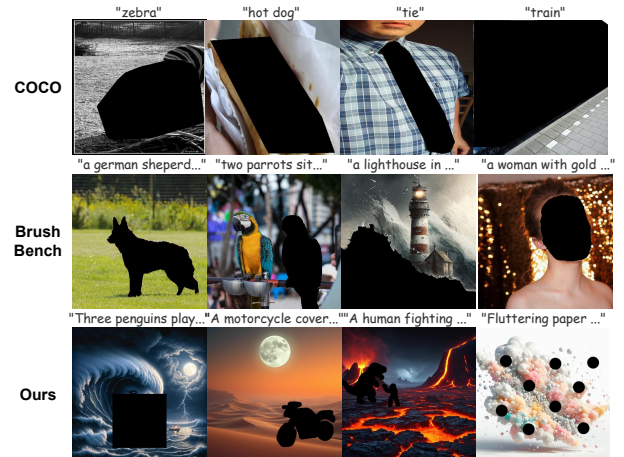


Figure 13. An illustration of evaluation data for T2I inpainting task.

	COCO [16]	BrushBench [13]	FCIBench
precise mask	O	O	O
complex prompt	×	O	O
rough mask	×	×	O
multi mask	×	×	O
context related	O	O	×

Table 3. Table of comparison cross different benchmark.

##### 7.2.1. COCO-Inpainting Benchmark

The COCO dataset, as a widely-used and well-annotated resource, has been adopted by many inpainting methods [20, 31, 42]. Different approaches utilize the COCO

dataset with varying strategies to better evaluate inpainting performance. Among these, we identified the open-source COCO-Inpainting Benchmark released by HD-Painter [20]. To ensure consistency, we randomly sample 600 instruction pairs from their benchmark, matching the size of BrushBench to minimize statistical bias.

The COCO-Inpainting Benchmark is based on COCO segmentation. The provided instructions are derived from ground-truth masks and corresponding labels. This context-driven setup better reflects the reconstruction capabilities of inpainting methods.

### 7.2.2. BrushBench

Recognizing the limitations of the COCO-Inpainting Benchmark, which focuses solely on real-world photographs and lacks creative instructions or human-made visual art, BrushBench was introduced. BrushBench is constructed using an automatic segmentation model SAM, which autonomously labels masks from the LAION-5B dataset. This process results in 600 well-defined inpainting instructions, providing a more diverse and creative benchmark.

### 7.2.3. FCIBench

FCIBench addresses three main limitations of the aforementioned datasets.

First, the input instructions in these benchmarks are derived from ground-truth captions, where the image itself already provides sufficient contextual hints to guide the generation process.

Second, the input instructions lack complexity. The COCO-Inpainting Benchmark only provides class labels, while BrushBench offers relatively concise captions. As a result, these benchmarks fail to evaluate performance on deep prompt-following tasks. These relative simple setting also reflected in the mask instructions, thus FCIBench introduce more diverse mask setting including “precise mask”, “rough mask” and “multi-mask”.

Lastly, both benchmarks raise significant concerns about training data contamination. As discussed in Erasing Concept from Diffusion Models (ESD), the memory effect of Stable Diffusion models is non-negligible. Since both benchmarks rely on ground-truth captions as test prompts and include datasets widely used during training, they are likely to suffer from data leakage. This issue undermines their ability to accurately reflect real-world performance.

These differences are provided and listed in Fig. 13 and Tab. 3.

### 7.3. IOU metrics

Observing the limitations of existing evaluation metrics in distinguishing between prompt-adherence and mask-following, increasing the size of the generated object also

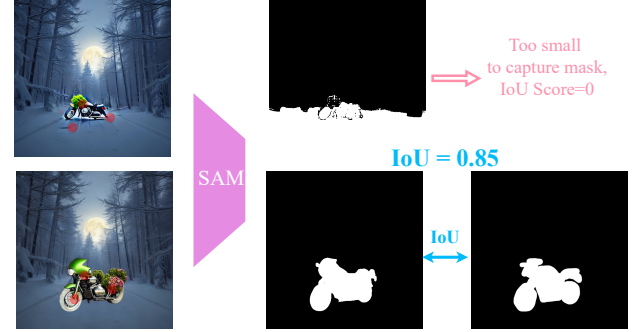


Figure 14. An illustration of the IoU Score calculation, the input kmmedoids points is denoted with red points.

	Fully masked	Partially masked	Not masked
Ratio	0.1773	0.3422	0.4805

Table 4. Table of masked ratio.

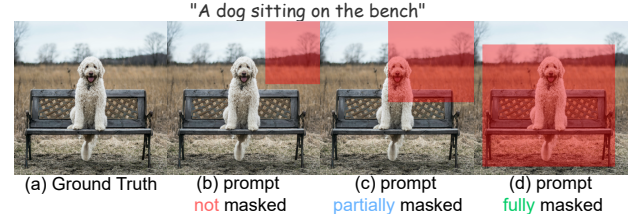


Figure 15. An illustration of possible training data generated by random mask strategy.

boosts the CLIP Score, even when the prompt is not followed precisely. Therefore, CLIP Score is not a reliable metric for measuring prompt-adherence alone, as it is also influenced by object size and other factors, as discussed in [5].

To disentangle the effect of object size from prompt-adherence, we introduce the IoU metric, calculated using auto-segmentation masks generated by SAM. This approach allows us to isolate prompt-adherence. For instance, if two outputs share the same IoU score, we infer that the output with the higher CLIP Score exhibits better prompt-adherence.

To compute the segmentation masks, we use SAM by inputting k-medoids points derived from the input mask. However, when the generated object is too small to accurately capture an IoU mask, we reject the segmentation mask if its area exceeds 1.5 times the input mask, setting the IoU score to zero. This process is illustrated in Fig. 14.



Figure 16. The result of applying the random mask strategy on the COCO dataset [16]. The white areas represent the object masks, while the red-boxed regions indicate the random masks, covering 25% of the image area.

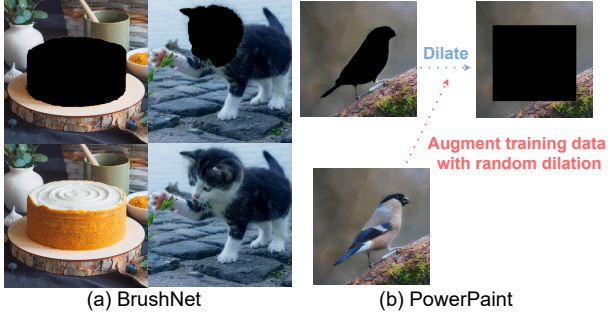


Figure 17. The illustration of segmentation based training strategy.

## 8. Training setting for inpainting models

### 8.1. Random mask strategy

As previously mentioned, the SDI model is typically trained on data processing using a random mask strategy, where 25% of an image’s area is randomly masked out. Although we cannot directly access the original training data, we employed the same random mask method on COCO val2017 dataset [16], which contains 4952 images with segmentation mask, and conducted a statistical analysis to examine its effects, as shown in Fig. 16.

We first calculated the average proportion of area covered by object masks within images in the dataset, which was found to be 32.2%. Consequently, when applying a random mask covering only 25% of the image, it is more likely to produce results similar to those shown in Fig. 15(b) and (c). Furthermore, we computed the mean Intersection over Union (mIoU) between the object mask and the random mask, obtaining a value of 0.2018, which further supports our hypothesis. Lastly, we analyzed the ratio of instances where objects were not fully masked versus fully masked, as shown in Tab. 4.

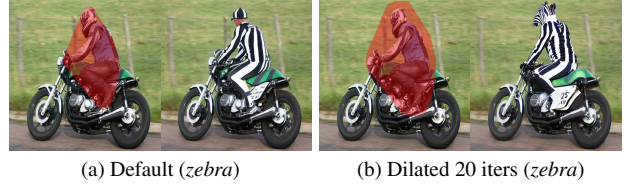
### 8.2. Segmentation mask strategy

The random mask strategy in the original SDI pipeline has been identified as a limitation, reducing its mask-fitting ability. To address this, methods such as SmartBrush [31], BrushNet [13], and PowerPaint [42] leverage the auto-segmentation tool SAM to facilitate the collection of segmentation mask data, as shown in Fig. 17. By exclusively utilizing segmentation data, these models learn a direct correlation between objects and prompt instructions.

However, a potential concern arises from the inherent biases of auto-segmentation tools. Since the segmented masks predominantly focus on objects, the models may struggle to generalize their use of background information. Furthermore, the fine-tuning process could potentially hinder the generalizability of the original model backbone. We also reported the computational time via RTX 3090 listed in Tab. 5.

Another widely adopted method, Blended Latent Diffusion (BLD) [1], relies entirely on the pretrained T2I backbone without requiring additional fine-tuning using masks. However, as highlighted in prior works [13, 20, 42], this approach exhibits extremely poor instruction-following capability, limiting its effectiveness in scenarios where precise control is essential.

## 9. Details for interpreting the mechanism behind SDI



### 9.1. Details of Settings in Sec. 3.3

In Sec. 3.3, we analyze the impact of input mask size on the generation outcomes. To simulate larger masks, we apply a dilation operation using a  $3 \times 3$  kernel with varying numbers of iterations.

As previously discussed, increasing the mask size potentially introduces more viable solutions that satisfy both the input instructions and the contextual constraints of the image. This phenomenon is illustrated in Sec. 9, where Fig. 18b demonstrates an output image that fulfills both the requirement of an object riding a motorcycle and the instruction to generate a zebra. This visualization aligns with and reinforces the quantitative findings and conclusions presented in Sec. 3.3.

	SDI [26]	CNI [39]	SDXL [23]	PP [42]	BN [13]	+HDP [20]	+FreeCond
Random mask training	O	O	O	O	X	-	-
Segmentation mask training	X	X	X	O	O	-	-
Estimated inference time	5s	7s	25s	8s	7s	*1.3	*1

Table 5. Overview comparison of different inpainting methods.

---

**Algorithm 1:** Compute self-attention heatmap for visualization

---

```

Input: Input Self-Attention Query  $Q \in \mathbf{R}^{N \times d}$ ,  

        Input Self-Attention Key  $K \in \mathbf{R}^{N \times d}$ ,  

        Flattened Mask Condition  $\bar{M} \in \mathbf{R}^N$ , where  

         $d$  is the number of feature channels  

Output: Attention Heatmap  $H \in \mathbf{R}^N$   

 $S = \text{Softmax}(QK^T)$  // Compute the  

        attention scores using softmax  

 $M_r = \text{torch.repeat}(M, N)$  // Repeat the  

        mask condition  $M$  to each q  

 $S_M = S \odot M_r$   $H = \text{torch.sum}(S_M, \text{dim} = -1)$   

        // Aggregate attention scores  

        along the last dimension  

return  $H$  // Return the computed  

        attention heatmap
    
```

---

## 9.2. Self attention visualization sudo code

In Sec. 3.4, we analyze the mechanism of the denoising UNet and conclude that convolutional down-sampling and self-attention mechanisms play a crucial role in propagating image-conditioned features into masked areas. To validate this hypothesis, we propose a self-attention visualization algorithm, detailed in Algorithm 1, which enables a clearer understanding of the ratio of features originating from within the masked area versus those from the surrounding regions.

## 9.3. Details of Discussion 3.3

To address the second research question, we analyze the differences between successful and unsuccessful prompt-following cases. Building on prior findings, we observe that increasing mask size enhances adherence to prompts. Since the text-to-image generation relies on CFG, we can observe how the noise is computed by Eq. (1) under different mask inputs. Recall that the final noise prediction  $\epsilon_\theta(z_t, t, p, \emptyset, w)$ , computed via CFG, is a weighted sum of two different noise predictions: the conditional prediction  $\epsilon_\theta(z_t, t, p)$ , and the unconditional prediction  $\epsilon_\theta(z_t, t, \emptyset)$ . The visualization of different noise predictions and corresponding image outputs is shown in Fig. 19. In the second row (c) and (d),  $\epsilon_\theta(z_t, t, p)$  exhibit a distinct variance distribution from  $\epsilon_\theta(z_t, t, \emptyset)$ , indicating an amplified diver-

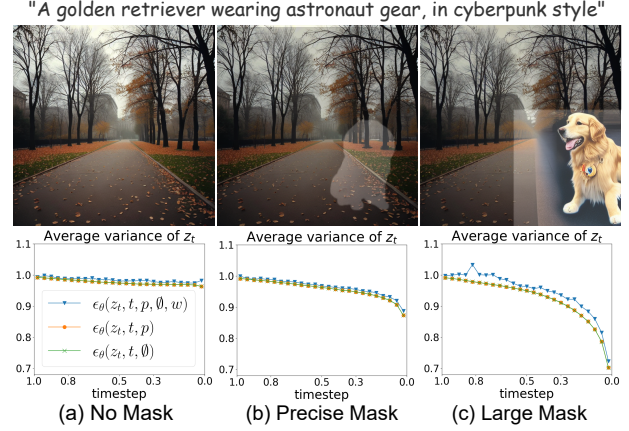


Figure 19. An illustration of different output images (row 1) and the variance of corresponding noise predictions (row 2). The input mask is highlighted by overlaying it onto the output images.

gence driven by cross-attention layers. We hypothesize that **specific dimensions of cross attention key are highly adapted to the mask input, selectively directing prompt information toward the masked region**. These kind of adaption can maintain both learned feature similarity, while amplifying the response inside masked area.

## 9.4. Channel influence indicator

### 9.4.1. Deeper case analysis

In the Sec. 3.4, we observe that the input mask  $M$  significantly impacts the channel-wise indicator differences. Since  $M$  is processed into both mask condition  $M^c$  and image condition  $z^c$ —which are the actual inputs passed to the denoising UNet—we aim to identify which of these inputs primarily drives feature shifts in the cross-attention layer. To isolate the effect of each input, we design three settings, each varying only one input condition. Notation follows that defined in Sec. 3.4. (The difference is **highlighted**)

- **Setting 1 (changing  $M$ ):**  $\Delta CI = CI(Q^l, M^l, k, i) - CI(Q^n, M^l, k, i)$
- **Setting 2 (changing  $M^c$  only):**  
 $Q^{s2} = W_Q \Phi_0(concat([z_t, M^l, z^n]))$  and,  
 $\Delta CI = CI(Q^{s2}, M^l, k, i) - CI(Q^n, M^l, k, i)$
- **Setting 3 (changing  $z^c$  only):**  
 $Q^{s3} = W_Q \Phi_0(concat([z_t, M^n, z^l]))$  and,  
 $\Delta CI = CI(Q^{s3}, M^l, k, i) - CI(Q^n, M^l, k, i)$

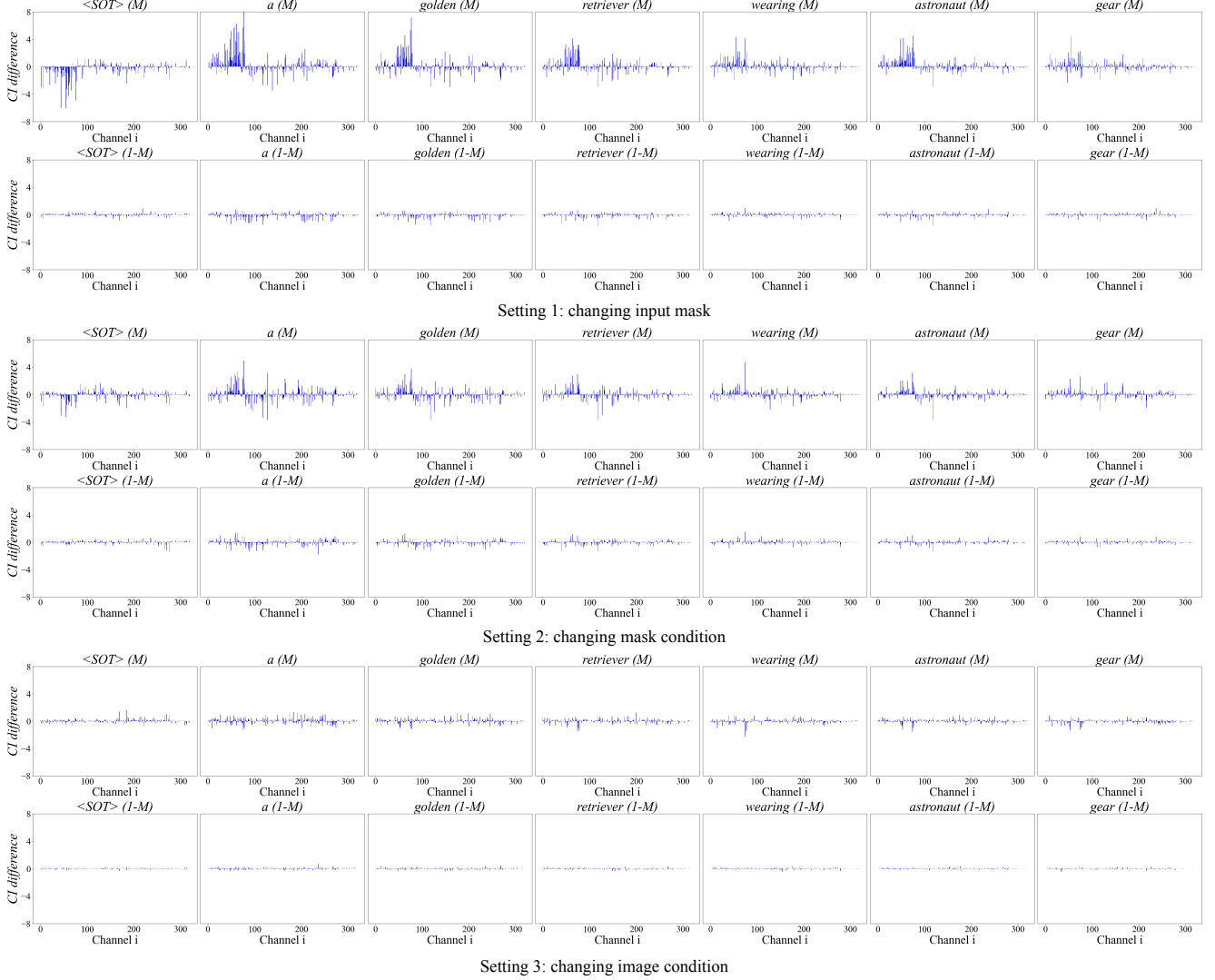
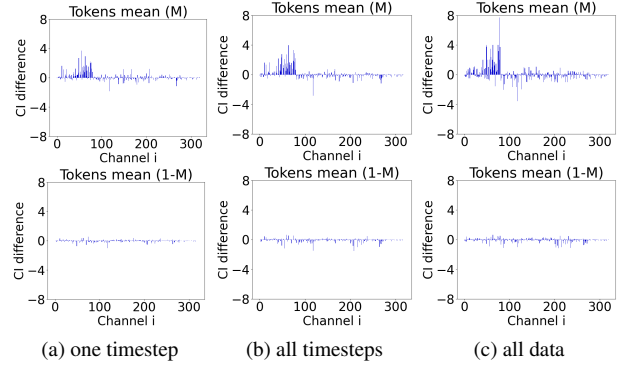


Figure 20. Comparison of  $\delta CI$  for three different cases. As illustrated, both  $M^c$  and  $z^c$  contributed to the change in  $\delta CI$ , but the influence of  $M^c$  is more significant.

The result in Fig. 20 shows that Setting 1 induces the largest difference in  $\Delta CI$ , with Setting 2 showing a similar effect, while the influence from  $z^c$  in Setting 3 is marginal. This aligns with the intuition that  $z^c$  and  $M^c$  jointly impact the denoising UNet output, producing the most substantial result when combined. Since  $z^c$  captures the overall image context, embedding the mask information in  $M^c$  offers better control over feature shifts in the cross-attention layer without disrupting the original image representation.

#### 9.4.2. More comprehensive analysis

To investigate the channel-wise feature adaptation effect in the cross-attention query and key mechanisms, we hypothesize that this phenomenon may not be limited to a specific case. To validate this hypothesis, we conduct a comprehensive evaluation across multiple scenarios to demonstrate that feature adaptation is a general behavior. Specifically,



hensive evaluation across multiple scenarios to demonstrate that feature adaptation is a general behavior. Specifically,

our experiments include:

- The average  $\Delta CI$  of all non-<SOT> and all non-<EOT> tokens, with results shown in Fig. 21a.
- The average  $\Delta CI$  of all non-<SOT> and all non-<EOT> tokens across all timesteps, with results shown in Fig. 21b.
- The average  $\Delta CI$  of all non-<SOT> and all non-<EOT> tokens across all timesteps and data samples in FCIBench, with results shown in Fig. 21c.

These results consistently reveal the presence of cross-attention feature shifts under different testing scenarios, supporting our hypothesis that **certain channels within the cross-attention layer are highly adapted to the mask input**. This adaptation not only ensures selective inpainting within the masked region but also preserves the original representational power of the pre-trained backbone, as only specific channels are influenced by the mask input, while the rest remain unaffected.

## 10. Details for FreeCond Method

### 10.1. FreeCond algorithm

The algorithm of FreeCond method discussed in Sec. 4, is shown in Algorithm 3. Noteworthy, our proposed FreeCond method is generalized from the original inpainting noise prediction function discussed in Sec. 3.1. Therefore, FreeCond can be flexibly included into other noise schedulers, architecture, which share similar input ( $M^C, z^c$ ).

Considering that  $LPF$  can be activated only during the early steps, we propose enabling the  $\alpha$  and  $\beta$  controls either exclusively in the early steps or in the later steps. To achieve this, we extend the original FreeCond control into a more general and flexible framework, as described in Algorithm 4. This strategy strikes a better balance between the different aspects of FreeCond control. Specifically, by introducing  $z^{fc}$  in the early steps, we enhance the generation of a mask-fitting low-frequency structure for the object. Subsequently, by incorporating  $M^{fc}$  in the later steps, we refine this low-frequency structure with more prompt-adherent details.

### 10.2. Merging FreeCond into Existing Models

Although the architectures of different models vary, **their similar input patterns lead to comparable feature representations, as confirmed by our experimental results**. Since our modifications only involve the mask condition  $M^c$  and image condition  $z^c$ , we focus on how each method processes these inputs. (In the following discussion, “SD” refers to the original Stable Diffusion model, and “SDI” refers to its inpainting variant.)

---

#### Algorithm 2: latent LPF

---

**Input:** Image latent  $z \in \mathbb{R}^{H \times W \times 4}$ , LPF threshold  $\gamma$   
**Output:** Filtered RGB Image  $I_{\text{filtered}}$   
**foreach** channel  $c \in \{0, 1, 2, 3\}$  **do**  
    Perform 2D FFT on channel  $c$ :  $\mathcal{F}_c = \text{FFT}(z_c)$   
    Create a low-pass filter mask  
     $M_{\text{LPF}} \in \{0, 1\}^{H \times W}$  such that:  

$$M_{\text{LPF}}(u, v) = \begin{cases} 1 & \text{if } \sqrt{u^2 + v^2} \leq \gamma \\ 0 & \text{otherwise} \end{cases}$$
  
    Apply the low-pass filter:  $\mathcal{F}_c^{\text{filtered}} = \mathcal{F}_c \odot M_{\text{LPF}}$   
    Perform the inverse FFT:  

$$z_c^{\text{filtered}} = \text{IFFT}(\mathcal{F}_c^{\text{filtered}})$$
  
**end**  
    Combine filtered channels to form the output:  

$$z_{\text{filtered}} = \text{Concat}(z_0^{\text{filtered}}, z_1^{\text{filtered}}, z_2^{\text{filtered}}, z_3^{\text{filtered}})$$
  
**return**  $z_{\text{filtered}}$

---

#### Algorithm 3: FreeCond control in inpainting model (DDIM scheduler for example)

---

**Input:** text prompt  $p$ , image condition  $z^c$ , mask condition  $M^c$ , inner-mask scale  $\alpha$ , outer-mask scale  $\beta$ , LPF-threshold  $\gamma$ , LPF-timestep  $t^{fc}$   
**Output:** noise latent of inpaintin output  
 $z_T \sim \mathcal{N}(0, I)$   
 $M^{fc} = \alpha \cdot M^c + \beta \cdot (1 - M^c)$   
 $z^{fc} = LPF(z^c, \gamma) // \text{ Algorithm 2}$   
**for**  $t = T, \dots, 1$  **do**  
    **if**  $t > t^{fc}$  **then**  
         $z_{t-1} = \sqrt{\bar{\eta}_{t-1}} \cdot \frac{z_t - \sqrt{1 - \bar{\eta}_t} \cdot \epsilon_\theta(z_t, z^{fc}, M^{fc}, t, p))}{\sqrt{\bar{\eta}_t}} + \sqrt{1 - \bar{\eta}_{t-1}} \cdot \epsilon_\theta(z_t, z^{fc}, M^{fc}, t, p))$   
    **end**  
    **else**  
         $z_{t-1} = \sqrt{\bar{\eta}_{t-1}} \cdot \frac{z_t - \sqrt{1 - \bar{\eta}_t} \cdot \epsilon_\theta(z_t, z^c, M^{fc}, t, p))}{\sqrt{\bar{\eta}_t}} + \sqrt{1 - \bar{\eta}_{t-1}} \cdot \epsilon_\theta(z_t, z^c, M^{fc}, t, p))$   
    **end**  
**end**  
**return**  $z_0$

---

#### 10.2.1. SDI only architecture (SDI, HDP [20], PP [42], SDXLI [23])

These methods handle  $M^c$  and  $z^c$  in the first convolution layer, where both conditions are concatenated with the input noise latent  $z_t$  before being passed into the convolution layer. Accordingly, we replace  $M^c$  and  $z^c$  with  $M^{fc}$  and

---

**Algorithm 4:** Stage FreeCond control

---

**Input:** text prompt  $p$ , image condition  $z^c$ , mask condition  $M^c$ , inner-mask scales  $\alpha_1, \alpha_2$ , outer-mask scales  $\beta_1, \beta_2$ , LPF-thresholds  $\gamma_1, \gamma_2$ , LPF-timestep  $t^{fc}$

**Output:** noise latent of inpaintin output

$$z_T \sim \mathcal{N}(0, I)$$

$$M^{fc1} = \alpha_1 \cdot M^c + \beta_1 \cdot (1 - M^c)$$

$$M^{fc2} = \alpha_2 \cdot M^c + \beta_2 \cdot (1 - M^c)$$

$$z^{fc1} = LPF(z^c, \gamma_1) // \text{Algorithm 2}$$

$$z^{fc2} = LPF(z^c, \gamma_2) // \text{Algorithm 2}$$

**for**  $t = T, \dots, 1$  **do**

**if**  $t > t^{fc}$  **then**

$$z_{t-1} = \sqrt{\eta_{t-1}} \cdot \frac{z_t - \sqrt{1-\eta_t} \cdot \epsilon_\theta(z_t, z^{fc1}, M^{fc1}, t, p))}{\sqrt{\eta_t}} + \sqrt{1-\eta_{t-1}} \cdot \epsilon_\theta(z_t, z^{fc1}, M^{fc1}, t, p))$$

**end**

**else**

$$z_{t-1} = \sqrt{\eta_{t-1}} \cdot \frac{z_t - \sqrt{1-\eta_t} \cdot \epsilon_\theta(z_t, z^{fc2}, M^{fc2}, t, p))}{\sqrt{\eta_t}} + \sqrt{1-\eta_{t-1}} \cdot \epsilon_\theta(z_t, z^{fc2}, M^{fc2}, t, p))$$

**end**

**end**

**return**  $z_0$

---

$z^{fc}$  before the first convolution layer.

### 10.2.2. ControlNet branch architecture (CN [39], BN [13])

The original ControlNet inpainting model introduces an additional ControlNet branch alongside the SDI backbone. We do not modify the input conditions of the ControlNet branch<sup>1</sup> but instead adjust the SDI backbone as described above.

BrushNet [13], on the other hand, utilizes the original SD model as its backbone and incorporates an additional BrushNet branch, similar to the ControlNet module, which takes  $M^c$  and  $z^c$  as input conditions. Therefore, we replace both  $M^c$  and  $z^c$  with  $M^{fc}$  and  $z^{fc}$  in BrushNet.

## 10.3. Qualitative Results of Changing FreeCond Hyperparameters

The qualitative results are shown in Fig. 22. First, in Fig. 22a, we observe that the introduction of  $z^{fc}$  reduces the influence of the background context, enabling the generation to focus more on the object. This adjustment leads to mask-fitting results, particularly evident in the FCI cases. For example, with the default setting  $(\pi, T)$ , only a small cat is generated while when  $z^{fc}$  is introduced, the generated objects align more closely with the mask instructions.

<sup>1</sup>The ControlNet branch uses  $I^c$  as its sole input condition, serving as a supplement to the SDI backbone.

However, when the low-pass filter (LPF) influence of  $z^{fc}$  becomes too strong, it can produce inharmonious outputs. This issue is apparent in settings such as  $(0.13\pi, 0.5T)$  and  $(0.13\pi, 0.2T)$  in the BrushBench case.

Secondly, regarding the influence of  $M^{fc}$ , we find that the  $\beta$  parameter of  $M^{fc}$  plays a crucial role in enhancing overall harmonization. This effect is especially pronounced in settings such as  $(0.7, 0.3)$ ,  $(0.7, 0.5)$ , and  $(1, 0.5)$  for the BrushBench case, where the generated dog faces appear more coherent and harmonious within the overall image. In contrast, the  $\alpha$  parameter of  $M^{fc}$  primarily affects prompt adherence. For instance, with a complex prompt like *a sleepy cat lounging on a cloud of cotton candy, in fairy-tale style*, varying  $\alpha$  not only ensures the appearance of the *cat* but also incorporates elements such as the *cloud of cotton candy* and *fairy-tale style*.

These qualitative results support our findings in Sec. 5.3, demonstrating that different FreeCond parameters influence distinct aspects of the noise prediction process. By adjusting these parameters, we can introduce various modifications to the original inpainting results.

## 11. Experimental detail

All the experiment are conducted with same random seed, and negative prompt, this prompt is modified from HD-painter ("word, bad quality, bad anatomy, ugly, mutation, blurry, error"), the pretrain weight and hyperparameter settings are follow the default setting provided by the open-source repository of each baselines<sup>2</sup>. For the FreeCond settings, we observe that different methods respond differently to FreeCond control, as discussed in Sec. 11.2. Through experiments with various settings, we assign tailored hyperparameters to each model. The quantitative results are summarized in Tab. 2, while the qualitative results are presented in Fig. 23, Fig. 24, and Fig. 25. The corresponding algorithm for utilizing these hyperparameters is detailed in Algorithm 4.

- **SDI:**  $(\alpha_1 = 1, \alpha_2 = 1.5, \beta_1 = 0, \beta_2 = 0.2, \gamma_1 = 0.75\pi, \gamma_2 = \pi, t^{fc} = 0.5T)$
- **CNI:**  $(\alpha_1 = 1, \alpha_2 = 1.5, \beta_1 = 0, \beta_2 = 0.2, \gamma_1 = 0.75\pi, \gamma_2 = \pi, t^{fc} = 0.5T)$
- **HDP:**  $(\alpha_1 = 1, \alpha_2 = 1.5, \beta_1 = 0, \beta_2 = 0.2, \gamma_1 = 0.75\pi, \gamma_2 = \pi, t^{fc} = 0.5T)$
- **PP:**  $(\alpha_1 = 3, \alpha_2 = 1, \beta_1 = 0.4, \beta_2 = 0, \gamma_1 = 0.75\pi, \gamma_2 = \pi, t^{fc} = 0.2T)$
- **BN:**  $(\alpha_1 = 0.7, \alpha_2 = 1, \beta_1 = 0, \beta_2 = 0, \gamma_1 = \pi, \gamma_2 = \pi, t^{fc} = 0.5T)$
- **SDXL:**  $(\alpha_1 = 3, \alpha_2 = 1, \beta_1 = 0.4, \beta_2 = 0, \gamma_1 = 0.125\pi, \gamma_2 = \pi, t^{fc} = 0.5T)$

<sup>2</sup>Therefore, we didn't include non-open source method Smart-Brush [31] into the experiment

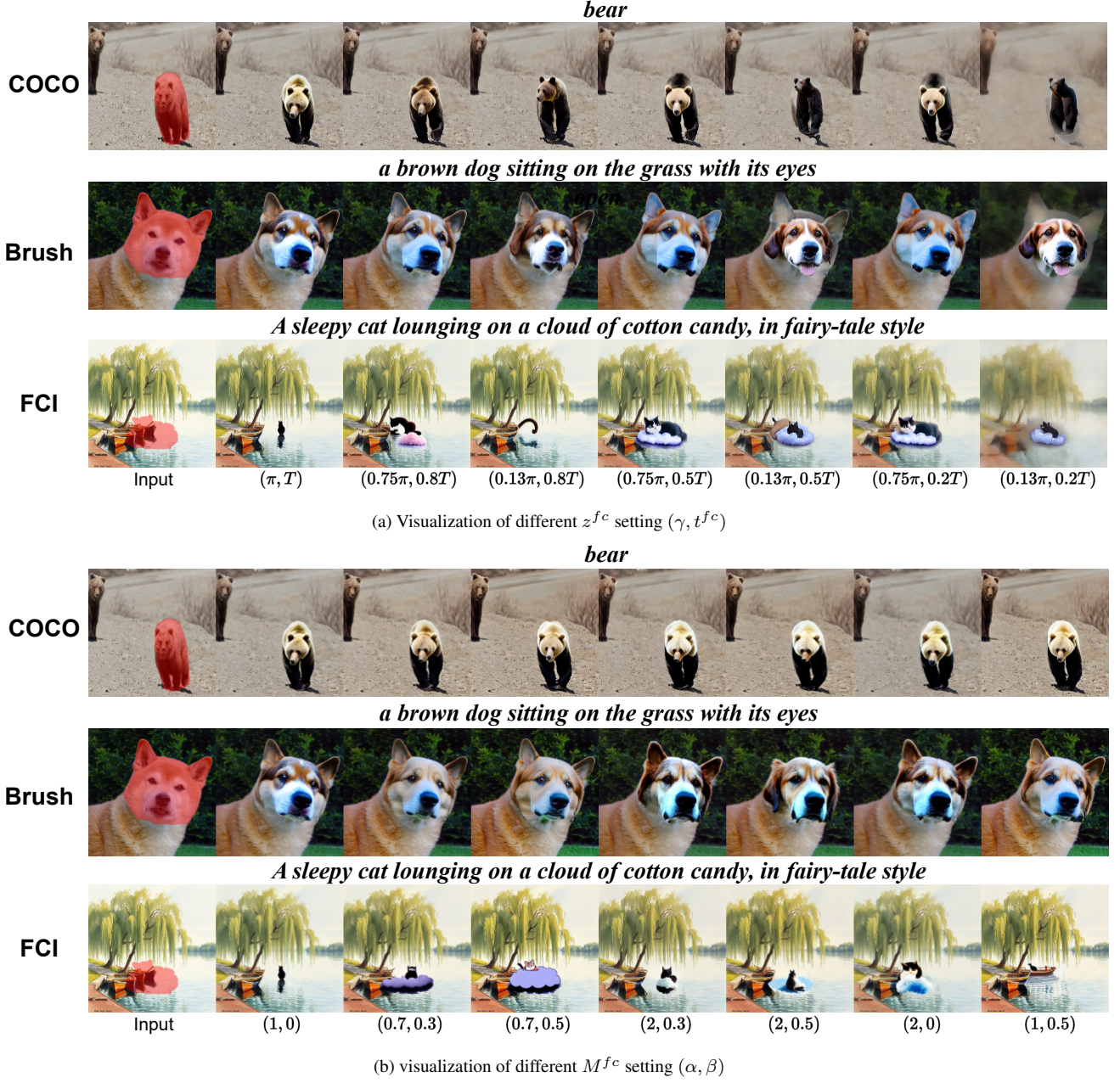


Figure 22. Qualitative visualization of FreeCond.

### 11.1. Qualitative Result

The corresponding qualitative comparisons of FreeCond are presented in Fig. 23, Fig. 24, and Fig. 25. In these figures, results without FreeCond control are shown in rows 1, 3, 5, and 7, while those with FreeCond control are displayed in rows 2, 4, 6, and 8.

To summarize, FreeCond effectively enhances the mask-fitting capability of random-mask-based methods (*i.e.*, SDI, CNI, HDP, and SDXL), achieving outputs that are more har-

monious, prompt-adherent, and mask-fitting. Although the improvements are less pronounced for segmentation-based methods (*i.e.*, PP and BN), FreeCond consistently enhances the harmony and prompt adherence of the originally generated results.

However, two issues are observed. First, when the instructions conflict (as shown in rows 1 and 2 of Fig. 23), where the mask input does not align with the prompt and the prompt conflicts with the image condition, the default FreeCond setting—designed primarily to enhance prompt

$t^{fc}$	FreeCond Control						Evaluation metrics						
	$\alpha_1$	$\alpha_2$	$\beta_1$	$\beta_2$	$\gamma_1$	$\gamma_2$	IR	HPS	AS	PSNR	LPIPS	CLIP	IoU
T	1	1	0	0	$\pi$	$\pi$	-1.95	0.17	6.69	25.54	0.06	11.45	0.07
0.5T	3	1	0	0	$\pi$	$\pi$	-1.63	0.19	6.62	25.07	0.06	15.20	0.23
0.5T	1.5	1	0	0	$\pi$	$\pi$	-1.90	0.18	6.68	25.46	0.06	11.75	0.09
0.5T	1	3	0	0	$\pi$	$\pi$	-1.68	0.18	6.62	23.73	0.08	14.69	0.26
0.5T	1	1.5	0	0	$\pi$	$\pi$	-1.94	0.17	6.70	25.36	0.06	12.40	0.13
0.5T	1	1	0.4	0	$\pi$	$\pi$	-1.80	0.18	6.72	24.89	0.06	13.17	0.13
0.5T	1	1	0.2	0	$\pi$	$\pi$	-1.94	0.18	6.73	25.28	0.06	11.69	0.13
0.5T	1	1	0	0.4	$\pi$	$\pi$	-1.88	0.18	6.73	24.23	0.06	11.92	0.10
0.5T	1	1	0	0.2	$\pi$	$\pi$	-1.90	0.18	6.70	25.24	0.06	11.62	0.08
0.5T	1	1	0	0	0.75 $\pi$	$\pi$	-1.35	0.20	6.41	24.85	0.07	17.91	0.50
0.5T	1	1	0	0	$\pi$	0.75 $\pi$	-1.60	0.17	6.07	22.06	0.24	17.97	0.42
0.5T	1	3	0	0.4	0.75 $\pi$	$\pi$	-1.24	0.20	6.45	22.62	0.10	18.68	0.61
0.5T	1	1.5	0	0.4	0.75 $\pi$	$\pi$	-1.25	0.20	6.41	23.90	0.08	18.10	0.53
0.5T	1	1.5	0	0.2	0.75 $\pi$	$\pi$	-1.29	0.20	6.44	24.58	0.07	18.27	0.54
0.5T	3	1	0.2	0	0.75 $\pi$	$\pi$	-1.42	0.19	6.60	24.20	0.08	17.00	0.35
0.5T	1.5	1	0.2	0	0.75 $\pi$	$\pi$	-1.37	0.20	6.46	24.66	0.07	17.66	0.47
0.5T	3	1	0	0.2	0.75 $\pi$	$\pi$	-1.36	0.20	6.56	24.03	0.08	17.50	0.39
0.5T	1.5	1	0	0.2	0.75 $\pi$	$\pi$	-1.33	0.20	6.46	24.60	0.07	17.86	0.52
0.8T	1	1.5	0	0.2	0.75 $\pi$	$\pi$	-1.69	0.19	6.66	25.06	0.06	14.01	0.21

Table 6. Quantitative results of stage version of FreeCond Algorithm 4, the default setting of original SDI is in gray, and the difference made by FreeCond are in blue and our final choice based on the FCIBench is in green

adherence and mask fitting—produces outputs that, while still following the instructions, are less harmonious. Second, as FreeCond is designed to adjust the model’s behavior rather than introduce new features, the outputs with FreeCond are similar to those without it, inheriting biases from the original generation, as shown in rows 7 and 8 of Fig. 25.

### 11.1.1. Qualitative results on FCIBench (Fig. 23)

Compared to the other two benchmarks, the instruction data in FCIBench are significantly more diverse. This complexity arises from both the prompt structure and the diverse mask shapes, which present challenges for mask fitting in most existing methods, particularly in rows 3 and 5. However, FreeCond effectively addresses these limitations, producing results that better adhere to the mask requirements.

Another challenge lies in the "style prompt." In most training data, style information is closely coupled with the image condition, and the entire image typically exhibits a single, consistent style. In contrast, FCIBench requires the model to generate objects with a style that is entirely distinct from the given image condition. As a result, the generated outputs often prioritize overall style coherence with the image condition at the expense of adhering to the style instruction, as seen in rows 1, 3, and 7.

With the support of FreeCond, this limitation can be mitigated, leading to more prompt-adherent results. However,

this emphasis on prompt adherence may occasionally disrupt overall harmony, necessitating case-by-case tuning by the user to achieve the desired balance.

### 11.1.2. Qualitative results on BrushBench (Fig. 24)

The BrushBench dataset primarily contains context-related inpainting pairs. As a result, the initial generated outputs tend to be more mask-fitting compared to those from FCIBench. Additionally, the prompt instructions in BrushBench are relatively simple, leading to prompt-adherent results in the initial generations. However, with the integration of FreeCond, the mask-fitting quality is further enhanced. This improvement is evident in rows 1, 2, 5, and 6, where the shapes of the house and dog align more closely with the mask instructions. Moreover, FreeCond improves prompt adherence and produces more harmonious outputs. For example, in rows 3, 4, 7, and 8, the generated content, such as the map and camera, aligns more accurately with the prompts.

### 11.1.3. Qualitative results on COCO-inpainting (Fig. 25)

As the COCO-inpainting dataset includes only simple object instructions, the impact of FreeCond is relatively minor. However, its benefits become significant when the mask input is relatively small, as demonstrated in rows 1, 2, 5, and 6, where missing objects such as the person and pizza are successfully generated with the guidance of FreeCond. Ad-

ditionally, FreeCond enhances the harmony of the generated objects compared to the original outputs, as shown in rows 3, 4, 7, and 8.

## 11.2. Hyperparameter discussion of FreeCond

To thoroughly evaluate the effect of FreeCond control across different methods and data distributions, we conduct a comprehensive set of experiments on various methods and benchmarks (Fig. 26, Fig. 27, and Fig. 28). These experiments analyze how different metrics change with varying FreeCond hyperparameters. The key finding is that FreeCond hyperparameters exhibit entirely distinct behaviors across the three data distributions and baseline methods, underscoring the importance of carefully tuning the hyperparameters for each specific case.

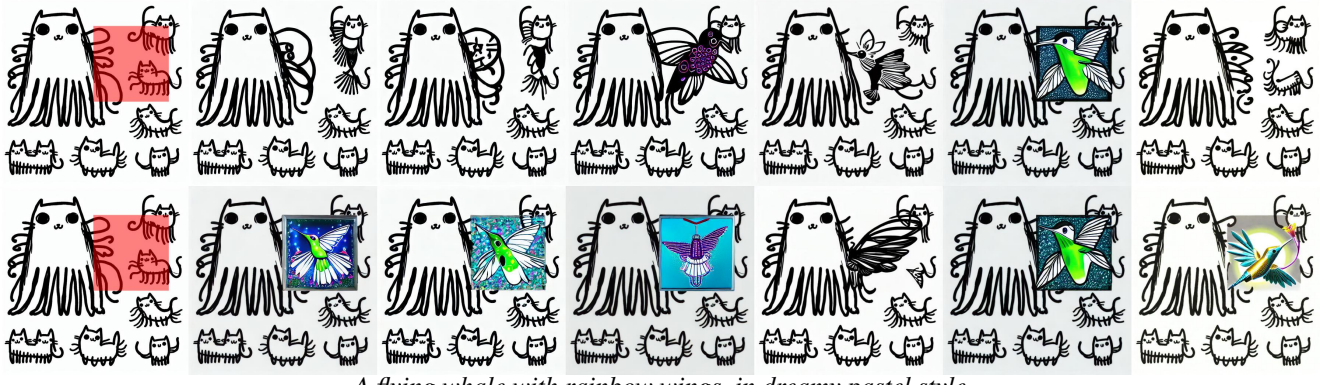
Nevertheless, as a training-free approach requiring no additional computation, FreeCond is well-suited for inference-time parameter tuning. From these plots, we observe that introducing  $z^{fc}$  generally increases both the CLIP score and IoU score, as evident in case (d). Adjusting  $\beta$  typically enhances image-quality metrics (*i.e.*, IR, HPS, AS), as shown in case (c). Similarly, modifying  $\alpha$  tends to improve both the CLIP score and IoU score as shown in (b). However, different methods respond differently. For instance, segmentation-based methods, such as PP and BN, exhibit similar patterns distinct from other methods.

These plots also provide insights into FreeCond’s usage with different baselines. For example, PP and BN often achieve better performance when  $\alpha$  is decreased to 0.7. Considering that case-by-case discussions may be biased and lack robustness, we refrain from further summarization or analysis.

## 11.3. Margin Hyperparameter (Tab. 6)

To balance instruction adherence and the model’s inherent capabilities, we introduce a more fine-grained control on the  $z^{fc}$  and  $M^{fc}$  across different timesteps, in Algorithm 4. From Tab. 6, we observe that directly merging  $z^{fc}$  and  $M^{fc}$  modifications at the same timestep often leads to suboptimal results. Instead, applying  $z^{fc}$  during the early timesteps is sufficient to improve both CLIP and IoU scores while minimally affecting background quality metrics. Furthermore, experiments demonstrate that using relatively small values for  $\alpha_2$  and  $\beta_2$  (*e.g.*, 1.5 and 0.2, respectively) further enhances nearly all evaluation metrics. For instance, when comparing configurations with  $\gamma_1 = 0.75\pi$ , the addition of  $\alpha_2 = 1.5$  and  $\beta_2 = 0.2$  achieves noticeable improvements. Based on these findings, we finalize our approach by employing  $z^{fc}$  during early timesteps to generate prompt-related objects and incorporating  $M^{fc}$  in later timesteps to refine prompt adherence, detail, and image quality.

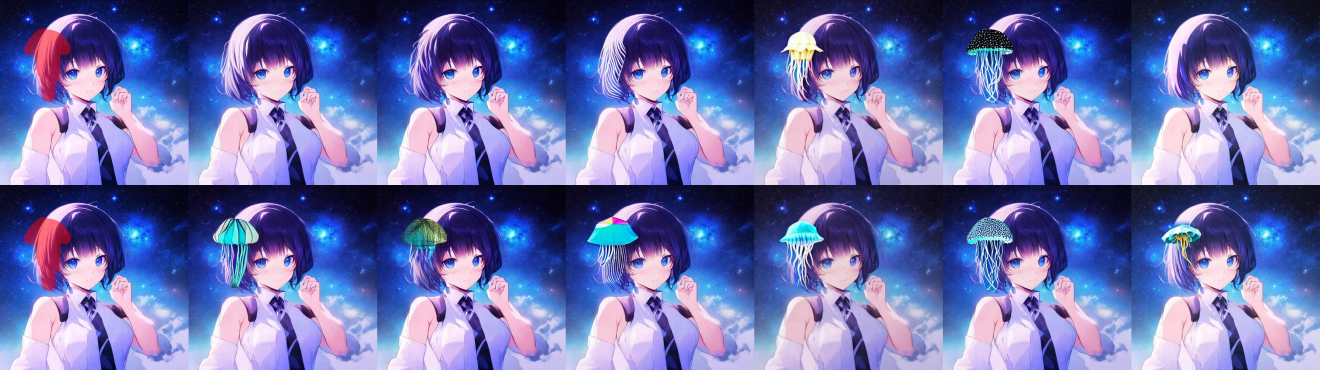
*A robotic hummingbird sipping nectar from a diamond flower; in futuristic metallic style*



*A flying whale with rainbow wings, in dreamy pastel style*



*A jellyfish made of floating origami paper, abstract art style*



*A dog and a cat facing each other, comic book style, full body*



**Input**

**SDI**

**CNI**

**HDP**

**PP**

**BN**

**SDXL**

Figure 23. Qualitative comparison of FreeCond in **FCIBench**. Results from the vanilla methods are displayed in the odd-numbered rows, while the corresponding results incorporating FreeCond are presented in the even-numbered rows.

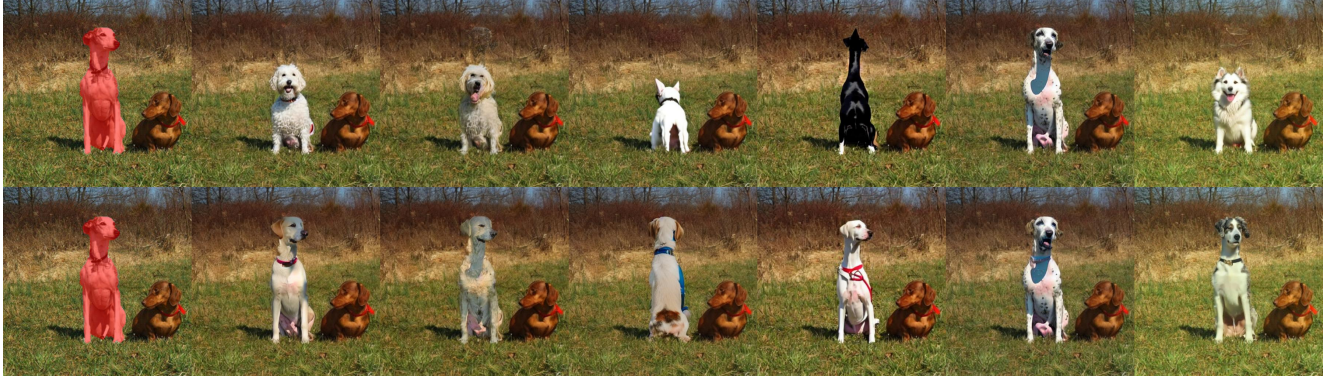
*a painting of a cabin in the snow with mountains in the background*



*a notebook, glasses and a camera on a map*



*two dogs sitting on the grass next to each other*



*a little girl playing a musical instrument*

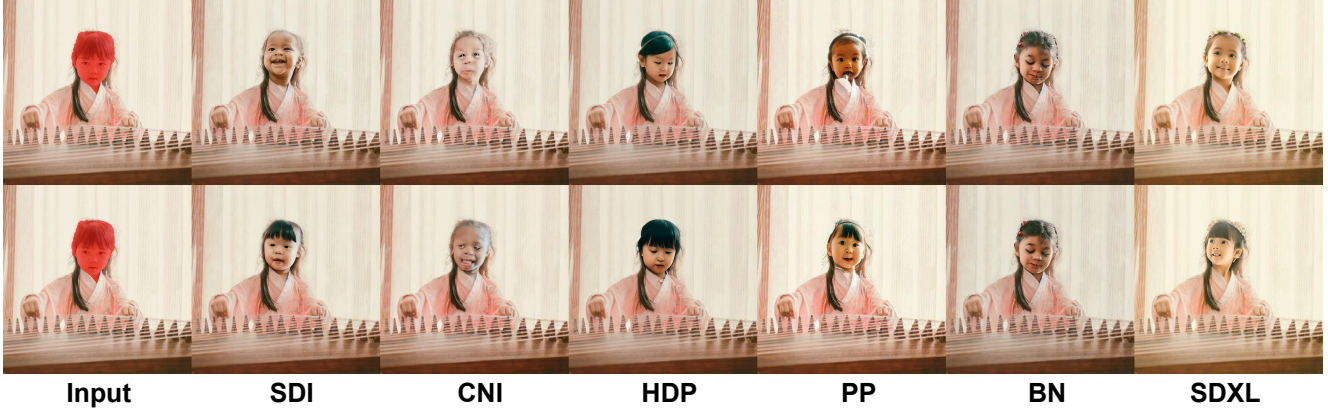


Figure 24. Qualitative comparison of FreeCond in **BrushBench**. Results from the vanilla methods are displayed in the odd-numbered rows, while the corresponding results incorporating FreeCond are presented in the even-numbered rows.

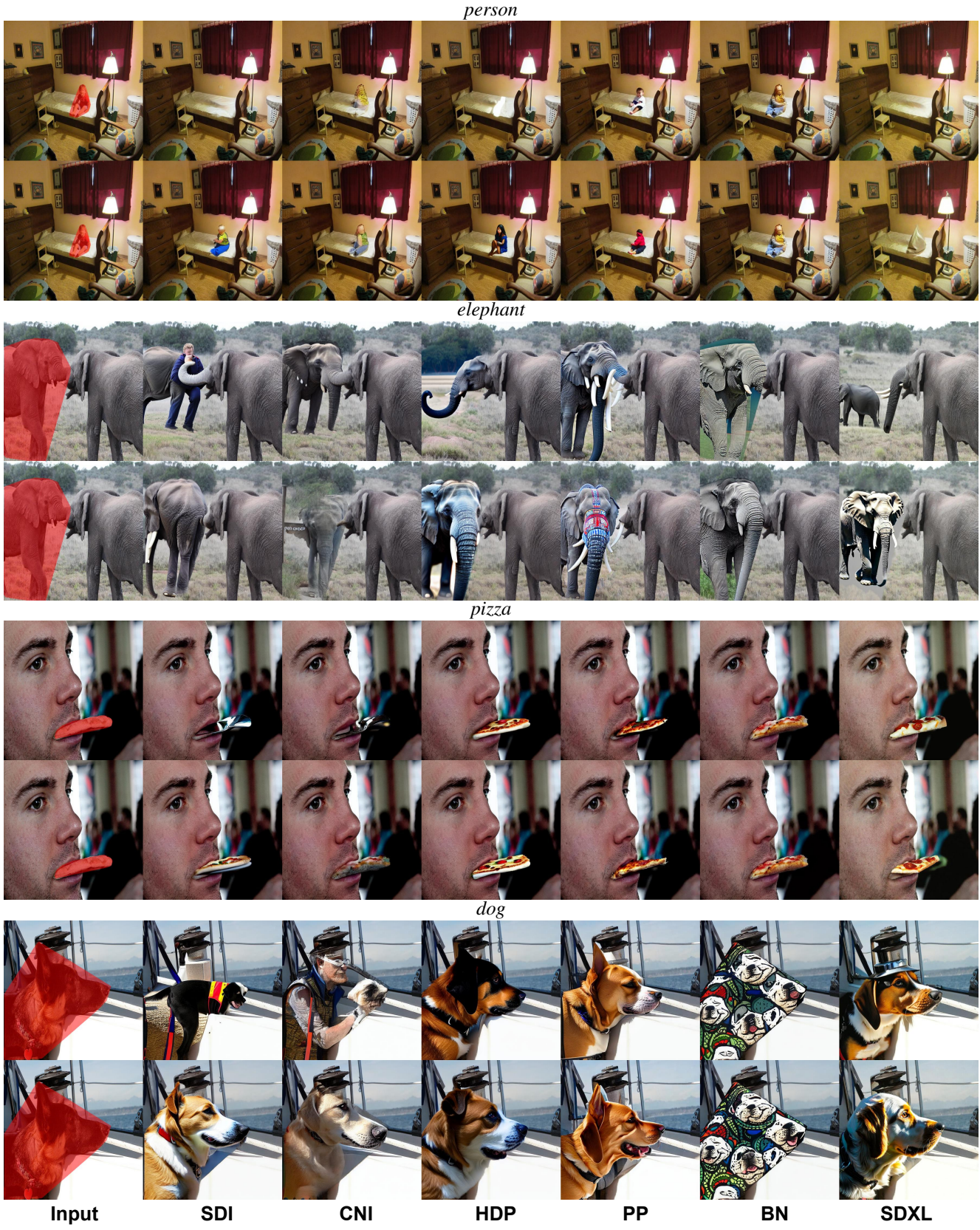


Figure 25. Qualitative comparison of FreeCond in **COCO-inpainting**. Results from the vanilla methods are displayed in the odd-numbered rows, while the corresponding results incorporating FreeCond are presented in the even-numbered rows.

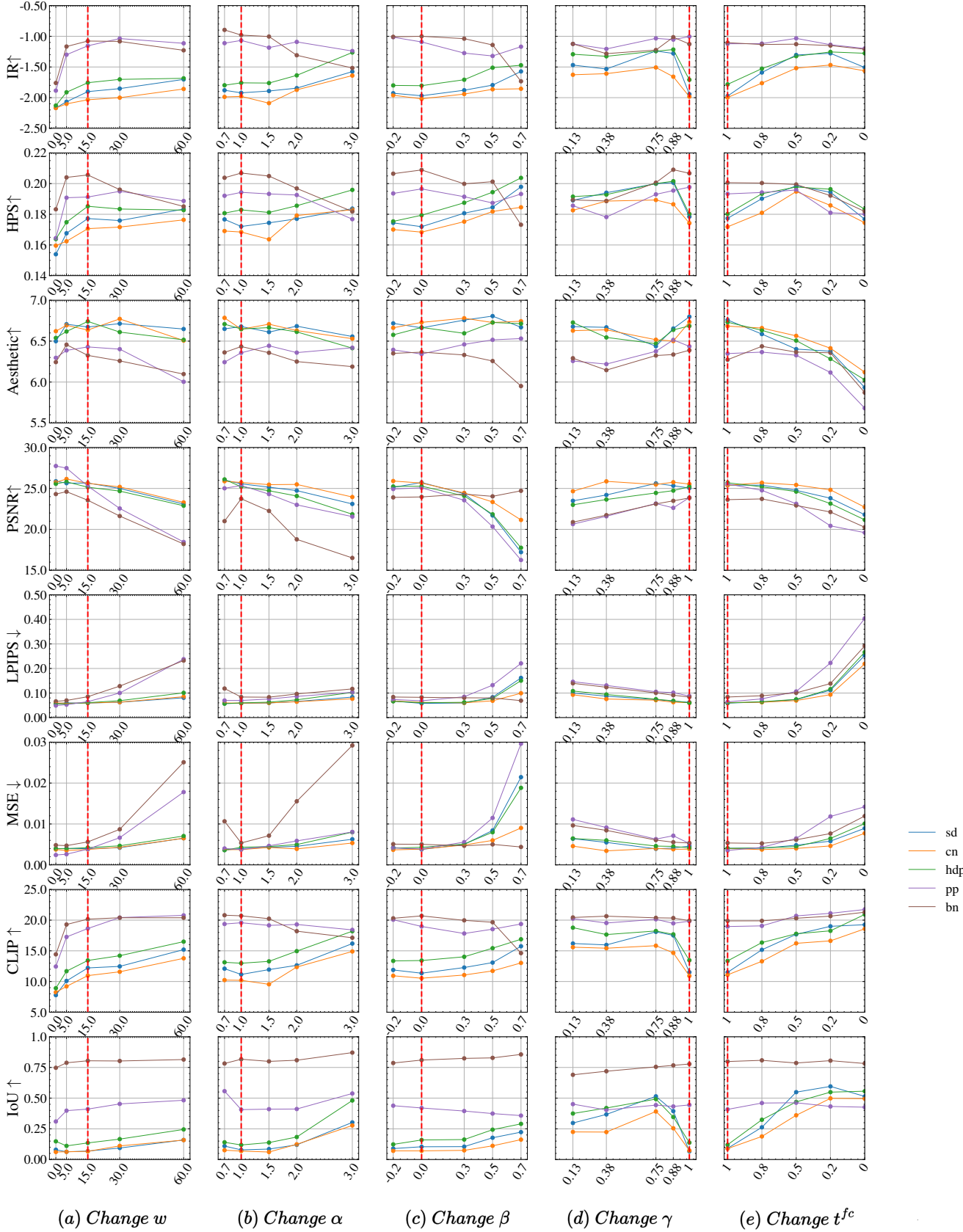


Figure 26. Sensitive test of hyperparameters on **FCIBench** (the default setting is highlighted with vline).

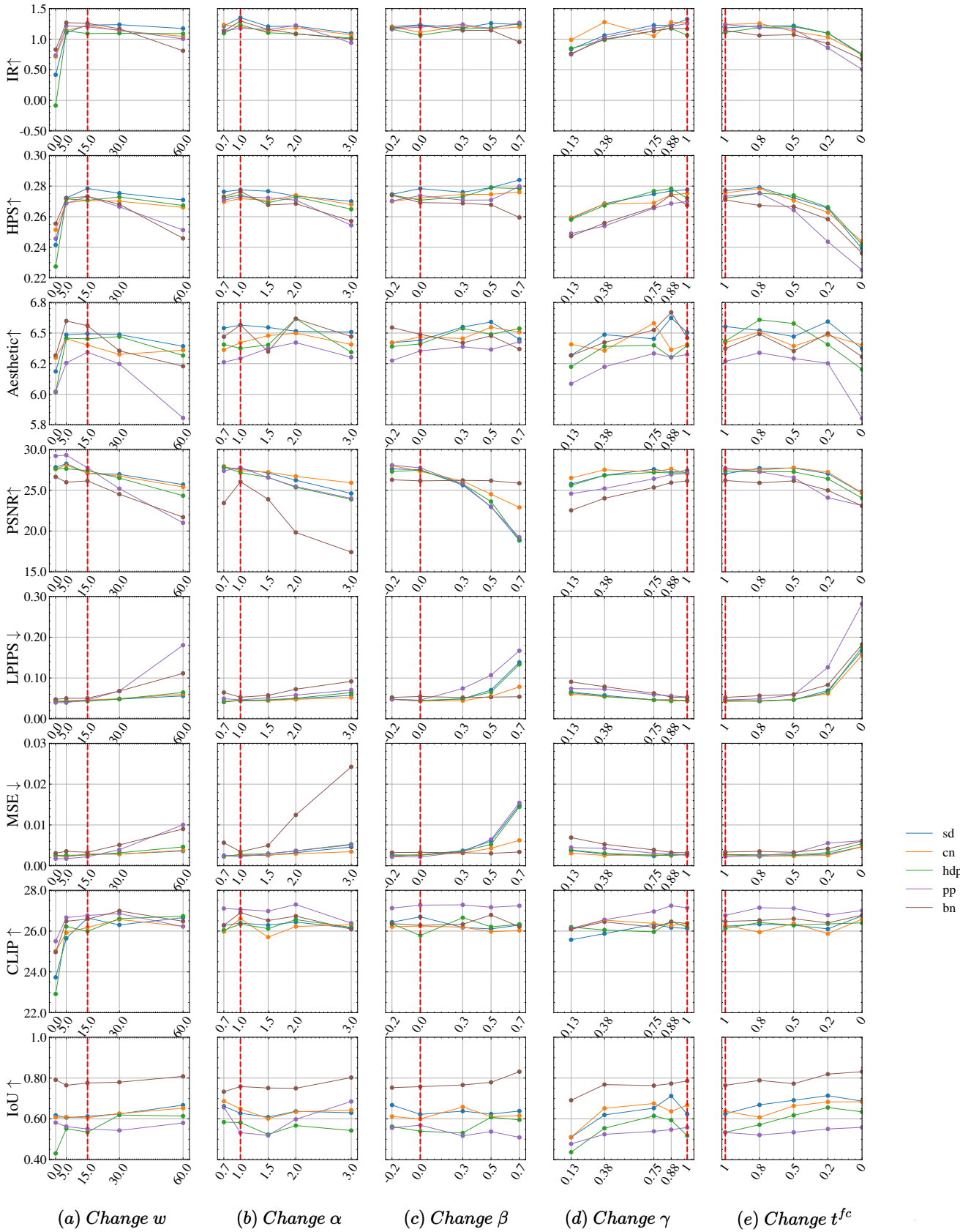


Figure 27. Sensitive test of hyperparameters on **BrushBench** (the default setting is highlighted with vline).

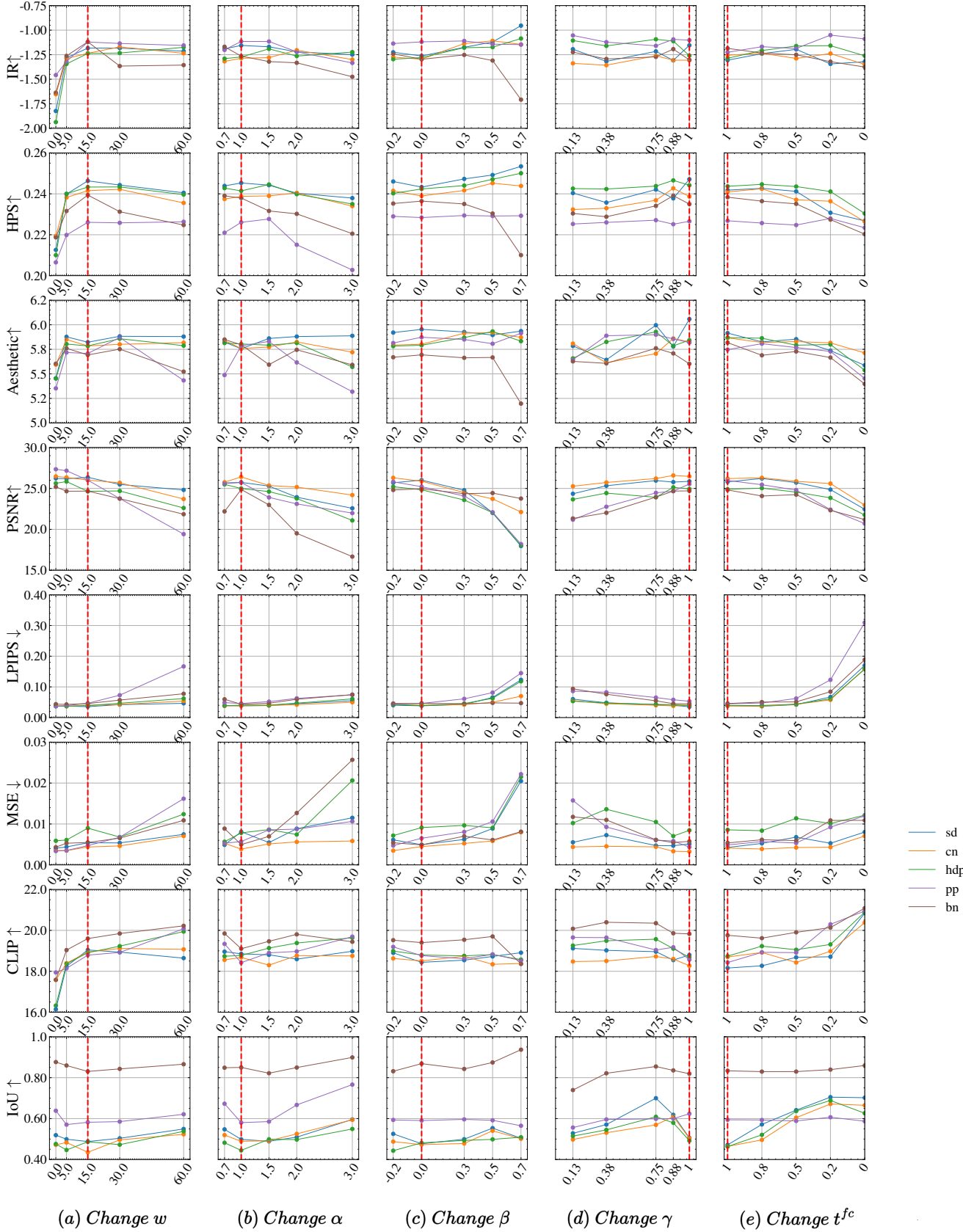


Figure 28. Sensitive test of hyperparameters on **COCO-inpainting** (the default setting is highlighted with vline).